Structural variability of the Tonga-Kermadec forearc characterised using robustly constrained geophysical data

Authors: Funnell M.J.[1], Peirce, C.[1] and Robinson, A.H.[1]

[1] Department of Earth Sciences, Durham University, South Road, Durham, DH1 3LE, UK.

Accepted Received in original form

Abbreviated title: Tonga-Kermadec forearc structural variability

Corresponding author:
Matthew Funnell
Department of Earth Sciences
Durham University
DH1 3LE
Durham
United Kingdom
Email: matthew.funnell2@durham.ac.uk

Structural variability of the Tonga-Kermadec forearc characterised using robustly constrained geophysical data

Funnell M.J.[1], Peirce, C. [1] and Robinson, A.H. [1]

SUMMARY

Subducting bathymetric anomalies enhance erosion of the overriding forearc crust. The deformation associated with this process is superimposed on pre-existing variable crustal and sedimentary structures developed as a subduction system evolves. Recent attempts to determine the effect and timescale of Louisville Ridge seamount subduction on the Tonga-Kermadec forearc have been limited by simplistic models of inherited overriding crustal structure that neglect along-strike variability.

Synthesis of new robustly tested seismic velocity and density models with existing datasets from the region, highlight along-strike variations in the structure of the Tonga-Kermadec subducting and overriding plates. As the subducting plate undergoes bend-faulting and hydration throughout the trench-outer rise region, observed oceanic upper- and mid-crustal velocities are reduced by ~1.0 km s^{-1} and upper mantle velocities by ~0.5 km s^{-1}. In the vicinity of the Louisville Ridge Seamount Chain (LRSC), the trench shallows by 4 km and normal fault throw is reduced by >1 km, suggesting that the subduction of seamounts reduces plate deformation. We find that the extinct Eocene frontal arc, defined by a high velocity (7.0-7.4 km s^{-1}) and density (3.2 g cm^{-3}) lower-crustal anomaly, increases in thickness by ~6 km, from 12 to >18 km, over 300 km laterally along the Tonga-Kermadec forearc. Coincident variations in bathymetry and free-air gravity anomaly indicate a regional trend of northward-increasing crustal thickness that predates LRSC subduction, and highlight the present-day extent of the Eocene arc between 32°S and ~18°S. Within this framework of existing forearc crustal structure, the subduction of seamounts of the LRSC promotes erosion of the overriding crust, forming steep, gravitationally unstable, lower-trench slopes. Trench-slope stability is most likely re-established by the collapse of the mid-trench slope and the trenchward side of the extinct Eocene arc, which, within the framework of forearc characterisation, implies seamount subduction commenced at ~22°S.

Key words: Controlled source seismology; Crustal imaging; Crustal structure; Subduction zone processes.

1 INTRODUCTION

Island arc-backarc systems record the characteristics of subduction over time as changes in sedimentary and crustal structures on the overriding plate (Dickinson & Seely 1979; von Huene & Scholl 1991; Reagan *et al*. 2013). Variations in the strength and roughness of the subducting plate are manifest as changes in the rate of frontal and basal subduction erosion (Clift & Vannucchi 2004; von Huene *et al*. 2004), and in the dominant stress regime acting on the overriding plate (Bonnardot *et al.* 2007). Although the trench-proximal regions of erosive

margins are typically controlled by the removal of material, new crustal and sedimentary material is also generated and distributed along active volcanic arcs (Clift *et al*. 1994; Clift *et al*. 1998; Watts *et al*. 2012). Forearcs continually evolve in response to these erosive and constructive processes, resulting in significant along-strike variations in sedimentary and crustal structures over the lifespan of the subduction system (Herzer & Exon 1985; Bonnardot *et al*. 2007; Contreras-Reyes *et al.* 2011).

West-dipping subduction initiated along the Tonga-Kermadec trench in the Eocene (Meffre *et al.* 2012; Michibayashi *et al.* 2012). Over the last ~50 Ma, the margin has evolved from a single arc into the complex series of arcs and backarc basins observed in the SW Pacific Ocean today (Fig. 1; Hawkins *et al.* 1984; Bloomer *et al.* 1995). The margin exhibits the most linear trench-arc structure and the highest convergence rates in the global subduction system (von Huene & Scholl 1991; DeMets *et al*. 2010). Subduction of the Louisville Ridge Seamount Chain (LRSC) at ~26°S separates the Tonga trench and forearc in the north from the Kermadec trench and forearc in the south (Lonsdale 1986; Ballance *et al.* 1989).

The subduction of large bathymetric anomalies, such as seamounts and aseismic ridges, results in accelerated erosion and complex deformation patterns (Lallemand *et al*. 1992; von Huene *et al*. 1997; Dominguez *et al*. 1998; Zeumann & Hampel 2015). Recent research into the nature and effects of LRSC subduction along the Tonga-Kermadec margin has generated a range of theories regarding the subducted ridge strike and location of collision onset. A westward bend in the strike of the chain, to varying degrees, has been proposed at the current trench-ridge intersection by Timm *et al*. (2013) and Bassett & Watts (2015), whilst others suggest or assume linearity of the bathymetric trend of the ridge into the subduction zone (e.g. Ruellan *et al*. 2003; Bonnardot *et al*. 2007; Stratford *et al*. 2015). Further uncertainty surrounds the onset location of LRSC subduction, which is proposed to be either at the northern end of the subduction zone (e.g. Ruellan *et al*. 2003; Bonnardot *et al*. 2007), or to the north of Horizon Deep Bight, ~22.5°S, where the Tonga trench exhibits an ~80 km trench offset (von Huene & Scholl 1991; Lallemand *et al*. 1992; Wright *et al*. 2000; Contreras-Reyes *et al*. 2011; Stratford *et al*. 2015). These contrasting theories imply that there are significant gaps in our understanding of how LRSC-subduction alters and deforms existing forearc structures.

In order to provide better constraint on the variability of existing forearc structures, and the effect LRSC subduction has on them, a comprehensive margin-wide forearc structural model is required. We present new wide-angle (WA) and multichannel seismic (MCS) data that image sedimentary, crustal, and mantle structure across the LRSC and Kermadec forearc, perpendicular to seamount chain strike. These data are synthesised with results from previously published geological and geophysical studies (e.g. Crawford *et al.* 2003; Contreras-Reyes *et al*. 2011; Meffre *et al*. 2012; Funnell *et al*. 2014; Stratford *et al*. 2015) as well as satellite-derived gravity anomaly data (Sandwell *et al.* 2014) to: i) constrain variations in the structure and deformation of the Pacific plate crust around the Tonga-Kermadec trench-LRSC intersection; ii) characterise along-strike variations in the inherited (pre-LRSC subduction) Tonga-Kermadec forearc crustal structure; and using these classifications, iii) determine the temporal and spatial extent of forearc deformation caused by LRSC subduction.

2 GEOLOGICAL SETTING

The Pacific plate subducts to the west along the ~2700 km-long, 020° trending, Tonga-Kermadec trench axis (Fig. 1). Evidence of volcanism throughout the Eocene (Bloomer *et al*. 1995), and as early as ~51 Ma (Meffre *et al.* 2012; Michibayashi *et al.* 2012), suggests that subduction initiation at this margin was concurrent with that along the Izu-Bonin-Mariana margin (Reagan *et al.* 2013). At the time of inception, volcanism was focussed along the now extinct Tonga arc, which forms the present-day forearc ridge (Fig. 1). Between 45 and 34-32 Ma, the forearc and arc subsided rapidly from a sub-aerial setting to ~3 km below the sea surface, causing the trenchward tilting of sedimentary intervals (Clift & MacLeod 1999). Subsequent to the initial period of volcanism, the Lau-Colville Ridge became the active arc and the South Fiji Basin opened until ~17 Ma (Herzer *et al.* 2011). During this period, seamount subduction is attributed with the arcward tilting of sediments and generating an erosional unconformity, prior to 16.2 Ma, on the Tonga forearc (MacLeod 1994; Clift & MacLeod 1999). At ~5.5 Ma, a shift in tectonic forces caused the opening of the Lau Basin and the Havre Trough (Ruellan *et al.* 2003), resulting in an apparent ~2 Myr volcanic hiatus and the migration of volcanism to the currently active Tofua and Kermadec arcs (Clift *et al*. 1994; Bloomer *et al*. 1995), which are roughly parallel to the trench. Collision of the LRSC with the Tonga-Kermadec subduction system is suggested to have initiated 5-4 Ma or >7 Ma (Ruellan *et al.* 2003 and Timm *et al.* 2013, respectively), and is observed at ODP site 841 as an increase in the trenchward rotation of the forearc at ~1.5-0 Ma (Fig. 1 – MacLeod 1994; Clift & MacLeod 1999).

Stresses associated with Pacific plate subduction along the Tonga-Kermadec margin generate large extensional faults throughout the downgoing oceanic crust and upper mantle (Pelletier & Dupont 1990; Contreras-Reyes *et al.* 2011). Similar normal extensional faults observed along other trenches, e.g. Chile and Costa Rica, are proposed to enable hydration of the upper mantle (Ranero *et al.* 2003; Ivandic *et al.* 2010; Moscoso & Grevemeyer 2015), facilitating a reduction in the flexural rigidity of the subducting plate (Billen & Gurnis 2005; Arredondo & Billen 2012). The oceanic crust subducting along the Tonga-Kermadec trench formed along the Osbourn spreading centre (Fig. 1) roughly perpendicular to the present-day convergence direction (DeMets *et al.* 2010), prior to ~90 Ma (Billen & Stock 2000; Downey *et al.* 2007). Shortly after crustal formation, hotspot magmatism generated the bathymetrically prominent LRSC (Lonsdale 1988; Vanderkluysen *et al.* 2014). The relatively young host-plate age is associated with the highly intrusive nature of the seamount cores and limited crustal thickening observed at the northwestern end of the seamount chain (Contreras-Reyes *et al.* 2010; Richards *et al.* 2013). Volcaniclastic sedimentation supplements the <200 m of sediment cover that is typical for the southwestern region of the Pacific plate (Burns & Andrews 1973).

The structure of the overriding plate varies significantly with distance from the trench, and along the length of the Tonga-Kermadec margin (Fig. 1). Limited sediment cover (<100 m) and a steeply dipping (10–24°), highly irregular, basement characterises the lower-trench slope (Karig 1970; Ballance *et al*. 1999). Mid-slope basins are observed along the entire length of the subduction system, although they are less prominent directly north of the present-day LRSC-trench intersection point (e.g. Karig 1970; Ballance *et al*. 1999; Funnell *et al.* 2014; Stratford *et al.* 2015). Low seismic velocities of 3.5-4.0 km s^{-1} up to 5 km below seafloor, and pervasive

123 normal faulting observed in cores at ODP site 841 (Clift *et al.* 1994; Contreras-Reyes *et al*. 2011; Stratford *et al.*
124 2014) suggest that the lower- and mid-trench slopes are subject to significant extensional regimes controlled by
125 subduction erosion (von Huene *et al.* 2004; Sallares & Ranero 2005). Between the mid-trench slope and the active
126 volcanic ridge the extinct Eocene arc, known as the Tonga Ridge, is bathymetrically expressed from Vava'u, the
127 northernmost island in the Tongan island group, to ~28°S (Ballance *et al*. 1999; Contreras-Reyes *et al.* 2011).
128 South of ~28°S, the forearc is defined by ~2 km deeper, sediment filled basins (Karig 1970; Funnell *et al.* 2014).
129 The active Tofua and Kermadec arcs lie 170-200 km west of their respective trenches (Ballance *et al*. 1989), and
130 distribute volcaniclastic material into the surrounding forearc and backarc basins (Karig 1970). Active backarc
131 extension causes the separation of the Tonga and Kermadec arcs from the Lau-Colville backarc, with higher
132 spreading rates and more complex plate structure in the northern Lau Basin (Zellmer & Taylor 2001; Ruellan *et al.*
133 2003; Conder & Wiens 2011).

134 There are a number of major along-strike boundaries that delimit major structural and deformational
135 variations. South of 32°S an anomalous increase in trench depth is associated with a westward step in the forearc
136 and deepening of the mid-slope terrace (Karig 1970; Pelletier & Dupont 1990). Ballance *et al.* (1999) noted that
137 these features also coincided with a marked change in backarc basin structure, with steeper basin-bounding faults
138 to the south and the seafloor reaching ~500 m deeper. This feature has been attributed to different mechanisms:
139 the initial point of Hikurangi Plateau subduction (Collot & Davy 1998), increased subduction erosion (Pelletier &
140 Dupont 1990; Ballance *et al.* 1999), and the southern extent of the extinct Tonga Ridge (Bassett *et al.* 2016).

141 Further north, subduction of the LRSC enhances subduction erosion (Ballance *et al*. 1989), causing the
142 Tonga trench to shift westward by ~80 km (Clift & MacLeod 1999). This process is thought to have formed
143 Horizon Deep Bight, the deepest part of the Tonga trench, and the steepest lower-trench slope, >10°, immediately
144 north of the present-day seamount subduction region (Fig. 1; Lonsdale 1986; Contreras-Reyes *et al*. 2011). The
145 active region of LRSC subduction-associated forearc deformation lies roughly arcward of Osbourn seamount, the
146 oldest bathymetrically expressed seamount in the chain. The deformation is indicated by a shallowing of the
147 trench axis by ~4 km (Ballance *et al*. 1989), forearc uplift of 300 m (Stratford *et al.* 2015), and the presence of a
148 gap in seismicity (Bonnardot *et al.* 2007).

149 At ~18°S a much smaller aseismic discontinuity coincides with the northern extent of the bathymetric
150 Tonga Ridge (Crawford *et al.* 2003; Bonnardot *et al.* 2007). Dredged rock ages decrease northwards across the
151 boundary (Meffre *et al.* 2012), and the backarc basin becomes increasingly complex with extension migrating
152 from the Eastern Lau Spreading Centre to the Central Lau Spreading Centre and Fonualei Rift (Zellmer & Taylor
153 2001; Ruellan *et al.* 2003; Conder & Wiens 2011).

154 **3 DATA ACQUISITION AND PROCESSING**

155 Profile B (Fig. 2), a coincident MCS and WA seismic line, was acquired during R/V Sonne cruise SO215
156 (Peirce & Watts 2011). East to west, the profile crosses Pacific crust and Canopus seamount, at ~65° from the
157 palaeo-spreading direction (Billen & Stock 2000), as well as the Kermadec forearc and arc south of the present-

158 day LRSC-trench intersection. Swath bathymetry and gravity data were acquired contemporaneously. Data from
159 Profiles A and D (Fig. 1), which were also acquired during cruise SO215, are further discussed in this paper
160 (Funnell *et al*. 2014; Stratford *et al*. 2015).

161 *3.1 Swath bathymetry data*

162 A hull mounted SIMRAD EM120 multibeam echosounder acquired depth soundings throughout the
163 transit and shooting phases of cruise SO215. This swath bathymetry dataset was cleaned to remove bad soundings
164 using MB-System (Caress & Chayes 1996), merged with swath data from previous cruises, and gridded at ~50 m
165 node spacings to provide good constraint on the depth of the seabed (Fig. 2). Expendable bathymetric-
166 thermographs, deployed at ~100 km intervals, recorded the seismic velocity of the water column to a depth of 1.8
167 km.

168 *3.2 Seismic data source*

169 Contemporaneous acquisition of the WA and MCS data required a 60 s shot interval to prevent water
170 wave wrap-around on the ocean-bottom seismographs (OBSs), whilst still achieving a reasonable MCS fold. The
171 seismic source consisted of a 12 G-gun array, with a combined volume of 5440 in^3 (84 l), towed 7.5 m below the
172 sea surface and fired at 3000 psi (210 bar).

173 *3.3 MCS data acquisition and processing*

174 MCS reflection data were recorded using a 3 km-long, 240-channel streamer with 12.5 m group interval,
175 that was towed at 10 m depth. At the average ship speed of ~4.5 kn, a shot spacing of ~150 m yielded a maximum
176 theoretical fold of 10. Given the low fold, 25 m super-bins were used for data processing, which increases the
177 average fold of cover from 10 to ~40 and significantly improves the reflectivity of the intra-sediment and
178 basement reflectors. Data were recorded at a 2 ms sampling interval in 59 s trace lengths.

179 A bulk time-shift of 548 ms corrected for the shot-receiver datum as well as aim point and shot triggering
180 delays. A Butterworth filter (bandpass: 3-10-100-120 Hz) reduced noise generated by the significant swell
181 encountered during SO215, increasing the SNR in the usable frequency bandwidth.

182 Initial processing of the MCS data involved detailed velocity analysis, undertaken at 50 CMP intervals
183 using semblance values as well as constant velocity gathers and stacks to generate a stacking velocity model with
184 1.25 km lateral resolution. Following the application of normal moveout correction and stacking, a finite
185 difference time-migration operator removed the strong scattered signal, particularly at the seabed in heavily
186 faulted regions. A seabed mute removed signal in the water column for display purposes.

187 *3.4 WA seismic dataset*

188 WA seismic data were recorded by 26 OBSs deployed ~15 km apart along Profile B, with a 30 km gap at
189 the Kermadec trench due to the maximum instrument depth rating of 8 km (Peirce & Watts 2011; Fig. 2a). A
190 hydrophone, vertical geophone, and two horizontal geophone components output analogue signals that were

digitised and recorded at 4 or 5 ms sampling intervals on the LC-type and KUM deep-water type instruments respectively.

Instrument-seabed coupling and variations in geological structures between source-receiver pairs control the SNR and the characteristics of seismic phases recorded by each instrument. Along Profile B the WA data are divided into three groups according to significant changes in these characteristics: OBSs 01-10 on the Kermadec forearc, 11-15 in the trench, and 16-27 on the Pacific plate.

3.4.1 Kermadec forearc OBSs 01-10

Sediment turning P-waves, P_s (2.2-3.5 km s^{-1}), are only observed on the westernmost instruments (01-04) on the Kermadec forearc, suggesting significant sediment accumulations are only located proximal to the Kermadec arc (Fig. 3). Further east, crustal arrivals, P_g (4.0-7.0 km s^{-1}), are observed as the shortest offset refractions (from ~4.5 km), suggesting poor sediment cover on the trench slopes. The SNR of crustal refractions on forearc instruments is highly variable, although, if they are observed, the arrivals are typically found at much greater offsets than those of the Pacific plate (up to 70 km offset). Mantle refractions, P_n (7.5-8.0 km s^{-1}), are less clear and are typically observed between 50-100 km offset.

3.4.2 Kermadec trench OBSs 11-15

Instruments located in the Kermadec trench display the most complex pattern of arrivals and the lowest SNR (e.g. Fig. 4). Crustal refracted arrivals indicate abnormally low velocities, between 3.5 and ~6.5 km s^{-1}, on the lower slope of the forearc. On the outer trench slope crustal velocities remain closer to those observed by the other Pacific plate OBSs (4.0-7.0 km s^{-1}). Incoming shots to trench-located instruments are observed to typical offsets for a given phase only if they pass through the plate on which the OBS is located. Signal that passes through the subduction interface is significantly attenuated, resulting in the rapid degradation of arrival clarity beyond the trench apex. As such, mantle refractions are rarely observed at this point along the profile and, although some rays appear to be transmitted between the overriding and subducting crustal units, these have a very high noise component.

3.4.3 Pacific plate OBSs 16-27

OBSs located on the Pacific plate recorded low-velocity (4.0-5.0 km s^{-1}) crustal turning rays as the shortest offset refractions (Fig. 5). No sediment arrivals were observed on the Pacific plate instruments due to the relatively thin sediment cover. Instruments located close to, or on, Canopus seamount display crust and mantle arrivals that are perturbed in time by the highly undulatory seafloor. Mantle turning arrivals are observed between 30 and <190 km offset from the instruments.

3.4.4 Pick method and uncertainty assignment

First and secondary arrivals were picked on either the hydrophone or vertical geophone record for each instrument, depending on which component displayed the higher SNR. Pick phases were assigned based on the offset and apparent velocity of the arrivals.

Pick uncertainties were calculated independently for each OBS based on instrumentation and location errors, as well as the qualitatively assessed SNR for a given pick. Assigned uncertainty values typically increase with shot-receiver offset, and thus turning depth. Instruments located in and around the trench had particularly high location errors due to the extreme water depth and strong water column current, and a low SNR due to the increased sub-seabed complexity (Table 1).

3.5 Gravity data acquisition

Gravity data were acquired port-to-port using a Lacoste & Romberg Air-Sea gravimeter. These data were processed, incorporating Eötvös and drift corrections, and tied to absolute stations to calculate the absolute free-air anomaly (FAA). Crossover analysis gives an average root mean square misfit, and thus dataset uncertainty, of ~10 mGal which, although relatively high, is most likely generated by the high gravity gradients in the region (Peirce & Watts 2011).

4 2D MODELLING

4.1 Forward velocity modelling

Forward ray tracing was chosen as the primary velocity modelling technique for the OBS dataset (Table 1) because of the extreme lateral heterogeneity expected and typical of subduction zone velocity structure. Profile B OBS locations, shotpoints, and bathymetry data were projected from geographic coordinates into distance along profile (Fig. 6), for modelling using *rayinvr* (Zelt & Ellis 1988; Zelt & Smith 1992).

4.1.1 Model initialisation and modelling method

The velocity model was initialised with the water column thickness and velocity along the profile, determined from high-resolution swath bathymetry and expendable bathymetric-thermograph data respectively. OBS instrument locations were refined in the model space by relocating instruments laterally and vertically to reduce the misfit between the modelled and observed water wave arrivals. Initial sediment layer velocity and thickness were derived from the first-pass processed stacking velocities and the interpreted basement reflector from the MCS data (Fig. 2b), and draped beneath the model seabed. Below this, a simple velocity gradient was applied down to the bottom of the model.

Improvements to the fit between the calculated and observed arrival times were achieved by iteratively changing either the depths of model layer boundaries or the velocities at the top and bottom of that layer, following the method of Zelt & Smith (1992). This approach was first applied to the shallow layers (i.e. the sediment column), improving the fit on a subset of instruments in a rolling window along the length of the model before moving onto deeper layers. Additional boundary nodes and layers were only added to the model when an acceptable fit could not be achieved with the existing model elements. Nodes are typically spaced at 2.5 km intervals for the seabed and sediment column, 5 km for the intracrustal layers, and >10 km at the Moho. In regions where the ray coverage was poor, such as through the sediment column or at the model edges, the model was kept as close to the background structure as possible.

259 *4.1.2 Misfit minimisation and the final velocity model*

260 Following the achievement of a reasonable qualitative agreement between the modelled and observed
261 datasets, the traveltime root mean square residual, T_{RMS}, and uncertainty-weighted factor, χ^2, enabled further
262 model improvements to be made within the uncertainty limits of observed data. The T_{RMS} and χ^2 misfits for
263 specific phases in the major regions of the model are presented with the pick uncertainties in Table 1. Areas of the
264 model with higher misfit, such as the trench-proximal region (T_{RMS}=113 ms) and the lower crust of the forearc
265 (T_{RMS}=83 ms) coincide with groups of instruments that exhibit poor ray coverage or image more geologically
266 complex structures.

267 The final velocity model, shown in Fig. 6b, has a total T_{RMS} misfit of ~85 ms, and a χ^2<2. The model has
268 nine layers that represent distinct geological units: three crustal layers and a mantle block, for each of the
269 overriding and subducting plates, and a laterally continuous sedimentary layer.

270 *4.2 Forward model sensitivity testing*

271 Forward model fit sensitivity was tested by adjusting individual layer thickness, upper and lower
272 boundary velocity (variable velocity gradient), and bulk layer velocity (constant velocity gradient) until a pre-
273 defined misfit threshold is exceeded. A single threshold value for the entire model was found to allow regions of
274 relative geological simplicity and better fit, such as the Pacific plate, more variability before exceeding the limit
275 and thus appearing less sensitive than areas of the model that fit less well. This result can be misleading, so an
276 improved understanding of model sensitivity was obtained by also testing the three main regions of the model
277 separately, with more realistic thresholds chosen to match the set of instruments represented.

278 The results of the sensitivity tests, shown in Table 2, indicate that intra-crustal regions of both the
279 subducting and overriding plates are sensitive to relatively small changes in layer depth (~0.3 km), upper or lower
280 boundary velocity (~0.3 km s^{-1}), and bulk layer velocity (0.2 km s^{-1}). Although the forearc sediments are similarly
281 sensitive, the lack of turning arrivals through the Pacific plate sediments gives minimal control on the shallow
282 velocity structure (up to a 0.5 km s^{-1} shift in upper or lower seismic velocity). Conversely, the Pacific plate region
283 of the model is almost twice as sensitive to changes in Moho depth and upper mantle boundary velocity (0.5 km
284 and 0.3 km s^{-1} respectively) when compared to the forearc (0.7 km and 0.8 km s^{-1} respectively). Model sensitivity
285 in the measurable characteristics of the trench region is found to be roughly half that of the analogous features in
286 the overriding and subducting plates. For the remainder of this paper, significant layer thicknesses and velocities
287 determined from the forward velocity model will be quoted with the relevant layer sensitivity to indicate
288 confidence in the results.

289 *4.3 Inversion modelling*

290 We used the inversion method of Zelt & Barton (1998) as an independent modelling procedure to test the
291 reproducibility of long-wavelength velocity structure, the degree of modeller-bias, and resolution of the final best-
292 fit WA model (as in Zelt *et al.* 2003). Model perturbations were limited by a set of velocity constraints to prevent
293 geologically unrealistic alterations, and smoothed to minimise the acquisition geometry influencing the outcome.

The starting model had a 1.5 km-thick region of high velocity gradient, from 1.5-6.0 km s^{-1}, draped beneath the seabed representing the sediment column and shallow crust (Fig. 7a). Below this velocities increase, reaching 8.0 km s^{-1} at 15.0 km depth to represent a constant-depth Moho, although no first-order velocity discontinuity is imposed. This starting model, which was chosen because of the variability in crustal thickness along the profile, enabled the greatest modelling freedom within geological reality. We found that the optimal modelling process used two runs of five non-linear inversion iterations, with the inversion cell size reduced between the runs. During run 1, 10 km by 1 km inversion cells improved the larger-scale velocity structure of the model (Fig. 7b). This reduced the misfit to ~100 ms (χ^2=6.8), with the greatest misfit remaining on the overriding plate and in the trench. For run 2, 5 km by 0.5 km inversion cells refined small-scale and shallow structures, most notably in the overriding crust (Fig. 7c), resulting in a further reduction of the misfit to 70 ms (χ^2=3.1). The final inversion velocity model (Fig. 7c) displays a velocity structure that is broadly similar to the forward model (Fig. 7d) and, often noted in inversions, acquisition geometry-related smearing is absent. The Pacific crust and upper mantle are represented by typical oceanic-velocity structure, except for a poorly defined Moho (Fig. 7c). As with the forward model, Canopus seamount exhibits low velocities (<6.0 km s^{-1}) within the volcanic cone. In the overriding plate, the inversion model displays thick regions of low velocity in the shallow crust (<8.0 km-below seabed) and throughout the lower-trench slope crust (170-220 km-offset). Regions with poor ray coverage, such as the lower forearc slope (Fig. 7e), remained poorly fitting following run 2 but are broadly comparable to the forward model and remain within the indicated sensitivity values. The relatively high misfit of these regions is most likely due to model smoothing factors and the inversion cell sizes significantly exceeding the true scale of subsurface velocity variability (e.g. Zelt *et al.* 2003). Although the forearc Moho is very vertically diffuse, it appears to be ~2 km shallower between 70 and 150 km model offset for the inverse model relative to the forward model. The final forward velocity model remains our 'preferred' velocity model, because it is better constrained by additional data (MCS information and WA-reflected phases), is better resolved, and is more geologically representative. The inversion velocity model indicates the minimum structure required by the first arrival dataset and, thus, highlights the most robust features that are shared by both models (e.g. Zelt *et al.* 2003).

4.4 Inversion model resolution testing

Checkerboard testing of the final inversion velocity model, using a 5% velocity perturbation, determined the smallest structures resolvable by the acquisition geometry and model parameterisation (Zelt 1998). Fig. 7f indicates that velocity anomalies larger than 30 km by 3 km should be well resolved throughout regions of the model with >200 rays per forward node (Fig. 7e). In regions with particularly high ray coverage, such as in the mid-crustal region of the Pacific plate, structures as small as 20 km by 2 km may be resolvable (Fig. 7g). Ray coverage and the recovery of the input checkerboard are consistently poorest between 150 and 220 km offset, in the trench region. These results indicate that the internal velocity structure of LRSC seamounts may be recoverable with acquisition geometries similar to that along Profile B. Despite this, the checkerboard tests suggest that the velocity perturbations within the lower-trench slope region of the overriding crust are so poorly resolvable, due to the high pick errors and low ray density, that a velocity anomaly would have to be larger than

that expected to be generated by an entire intact seamount to be determinable. To achieve the accurate and robust imaging of such a feature, greater ray densities would be required, either through the addition of more instruments, or the addition of more shots in the region.

4.5 MCS reprocessing and fit to WA data

Although of a lower lateral and vertical resolution than the MCS stacking velocity model through the sediment column (1.25 km), the final WA forward velocity model (~2.5 km) should better represent true subsurface velocities. Conversion of the robustly tested and well resolved velocity model from depth to the time domain enabled the restacking and migration of the MCS dataset to produce a more geologically representative seismic section (e.g. Fig. 2d and f).

Restacking focused a band of deeper reflectivity beneath the flat-lying segments of the Pacific crust, at 9-10 s TWTT, that was previously unseen in the initial stack based on velocity analysis alone (compare Fig. 2e and f). This reflector fits to within 0.5 km of the forward velocity model crust-mantle boundary, suggesting it represents the Moho. The Moho reflector is not observed beneath the forearc due to the high amplitude water column multiple energy. The top-crust reflector fits within 0.1 km of the respective forward model boundary throughout the section except in the vicinity of the thicker upper forearc basin, which is most likely due to the scale of basement variations being below the lateral sensitivity of the forward modelling method. Despite the reduced lateral resolution and slight mismatch in the depth of the top-crust, there is no evident loss of the intra-sediment reflector information in the restacked MCS reflection data (Fig. 2d). This therefore provides further confidence that the WA velocity model is a good representation of the velocity structure of the crust along the profile.

4.6 *Gravity anomaly modelling*

The observed gravity anomaly provides an independent test of velocity model uniqueness and gives additional constraint on poorly resolved regions. The final forward velocity model was, therefore, converted into a density model consisting of 2D polygons. The expected free-air gravity anomaly was calculated from these using *grav2d*, based on the algorithm of Talwani *et al*. (1959).

Model edge effects were reduced by extending the density structure for 1000 km beyond the model edges, draped beneath the bathymetry extracted from the GEBCO 30 arc-second dataset (IOC *et al.* 2003). The inclusion of the subducting slab and mantle structure to 100 km depth, based on the extension of the velocity model using expected slab dips from slab1.0 (Hayes *et al.* 2012), removed the initial long-wavelength gravity anomaly mismatch.

A layered crustal block-model, where the average velocity through each layer of the forward velocity model determined the density of its respective block, generated the best-fitting gravity anomaly (Fig. 8). Standard velocity-density relationships were applied for the sediment column (Nafe & Drake 1957) and the subducting Pacific oceanic crust (Carlson & Raskin 1984), with a good fit found for the subducting plate. Continental (Christensen & Mooney 1995) and oceanic crustal velocity-density relationships were tested for the overriding

365 crust and, although both failed to generate the high-amplitude (~200 mGal) forearc anomaly, the oceanic crustal
366 relationship was found to produce the closest fit (~30 mGal). This suggests that the forearc crust may be of a
367 predominantly mafic, rather than felsic, composition. The addition of a high-density anomaly (3.2 g cm^{-3}) at the
368 base of the crust, coincident with the region of high velocity between 50 and 150 km model offset, significantly
369 decreased the misfit of the entire model to 12.9 mGal.

370 **5 COMBINED MODEL DESCRIPTION AND INTERPRETATION**

371 *5.1 Background Pacific plate*

372 Along Profile B the Pacific plate displays highly variable basement reflector depths (Fig. 2b). Sediment
373 thicknesses typical for the region of 100-200 m are only observed at ~410 km model offset and instead reach >1 s
374 TWTT (~1.5 km at 3.0 km s^{-1}) in the downthrown segment of a normal fault at ~415 km offset (Burns & Andrews
375 1973; Funnell *et al.* 2014). Despite this, typical oceanic crustal velocities are observed at the northeastern end of
376 Profile B (Fig. 9b). The oceanic crust is ~6.0 ± 0.3 km thick, consisting of an ~1.5 ± 0.3 km thick upper- and
377 middle-crust (3.5-6.5 ± 0.2 km s^{-1}), and a 4.5 ± 0.3 km thick lower crust that reaches 7.1 ± 0.3 km s^{-1} at the Moho.
378 Upper mantle velocities are consistently low, ~7.6 ± 0.3 km s^{-1}, compared to typical Pacific plate velocities of ~8.2
379 ± 0.3 km s^{-1} (Fig. 9b; Spudich & Orcutt 1980; White *et al.* 1992). The ~65° orientation of Profile B to the palaeo-
380 spreading, or fast seismic wave propagation direction of the Osbourn spreading centre (Fig. 1), may cause these
381 upper mantle seismic velocities to be close to the lower limit of what may be expected from typical azimuthal
382 mantle anisotropy of 4-7%, which is controlled by preferential olivine crystal alignment (Kodaira *et al.* 2014).

383 *5.2 Canopus seamount (LRSC)*

384 Sediments in the moat around Canopus seamount reach ~1.5 km thick, with reflectors typically dipping
385 away from the seamount. Although the sediment layer thickness was insufficient to observe or model turning rays,
386 the inferred average layer velocity of ~2.5 km s^{-1}, and internal reflectivity, suggests that the thick sediment
387 accumulation consists of volcaniclastic basalts and glass associated with seamount emplacement (Koppers *et al.*
388 2012; Vanderkluysen *et al.* 2014). Along Profile B, the internal velocity structure of Canopus seamount increases
389 from 3.0 to 5.5 ± 0.3 km s^{-1} over the first 5 km below the peak. These relatively low velocities suggest that the
390 shallow seamount structure imaged comprises highly porous extrusive and intrusive basaltic rocks more typical of
391 upper oceanic crust (White *et al.* 1992; Koppers *et al.* 2012). Contreras-Reyes *et al.* (2010) observed velocities of
392 6.4 km s^{-1} less than 2 km beneath the summit of the seamount immediately southeast of Canopus, and proposed
393 that they represent a highly intrusive mafic core. Although such high internal velocities are not observed on Profile
394 B, their absence could be explained as an artefact of sampling location and limited intrusion width, as Profile B
395 crosses the saddle between the two peaks of Canopus seamount (Fig. 2a). Elevated velocities of ~7.4 ± 0.3 km s^{-1}
396 at the base of the crust beneath the seamount are comparable to the seismic structures imaged at adjacent
397 seamounts (Contreras-Reyes *et al.* 2011; Stratford *et al.* 2015). These anomalously high velocities, and

corresponding slightly thickened crust, extend over 50 km from the seamount summits, suggesting that the LRSC seamounts are supported by broad lower-crustal intrusions (Contreras-Reyes *et al.* 2011; Richards *et al.* 2013).

5.3 Trench-outer rise region

Between Canopus seamount and the trench, bend-related normal faulting is manifest as <0.1-0.3 km trenchward-dipping reflector offsets that preserve a sub-horizontal seabed (Aubouin 1989; Ranero *et al.* 2003). This deformation pattern is significantly different to the 2.0 km-throw horst and graben structures observed on Profile D that coincide with an increased plate dip of ~5° (Fig. 10a & b; Funnell *et al.* 2014). Coincident with this region of faulting, between 0-55 km perpendicular distance from the trench, upper- and mid-crustal velocities are reduced by ~1.0 km s^{-1}, lower-crustal velocities remain unchanged, and upper mantle velocities decrease by ~0.3 km s^{-1} to ~7.4 ± 0.3 km s^{-1}.

5.4 Lower- and mid-trench slope

Large fault blocks and a rough seabed define the lower trench slope (Fig. 2a; Karig 1970). Sediment accumulations are limited to <0.1 s TWTT thick and are, for the most part, absent due to an ~10° slope. This region exhibits the lowest crustal seismic velocities in the model, increasing from 4.2 ± 0.6 km s^{-1} beneath the sediments to just over 6.0 ± 0.6 km s^{-1} at the base of the ~9 km-thick crust (Fig. 11c). The calculated gravity anomaly for the lower-trench slope only fits the observed data when densities derived from the local seismic velocity structure (i.e. kilometre scale) were ignored and, instead, entire forward model layers were converted into density blocks (Fig. 8), indicating that the velocity-density ratio that defines this model region is not typical of oceanic crust. Similar seismic wavespeeds and poor reflectivity are observed by Contreras-Reyes *et al.* (2011) and Sallarès & Ranero (2005) at the Tonga and North Chile margins respectively, and are attributed to the pervasive faulting, disaggregation, and hydration of the overriding crust in response to subduction erosion (e.g. Clift & MacLeod 1998; Clift & Vannucchi 2004).

Further west, between 160-170 km offset, an ~1.0 s TWTT (750 m-high) horst-and-graben structure offsets the lower-trench slope from a poorly imaged mid-slope sedimentary wedge. Sediments thicken to ~1.0 s TWTT and sedimentary reflectors tilt more arcward towards the east of the ~25 km-wide basin. Velocities of >6.0 km s^{-1} are reached just 4 km below the sediment base, and more typical lower crustal velocities are observed e.g. 6.8-7.2 ± 0.3 km s^{-1} (Holbrook *et al.* 1999; Contreras-Reyes *et al.* 2011).

5.5 Upper forearc slope and arc

Along Profile B, the upper forearc slope is defined by an ~50 km-wide ridge and basin in front of the active volcanic arc (Fig. 6a). The sediments beneath the ridge are ~1.0 s TWTT thick and relatively horizontal, although broken up by pervasive small-scale, <0.1 s TWTT throw, normal faults (Fig. 2c & d; Herzer & Exon 1985). In the ~40 km-wide basin, an ~2.0 s TWTT thick sedimentary succession is divided by a high amplitude intra-sediment reflector at ~1.0 s TWTT-below seafloor. This high amplitude reflector pinches out onto the basement of the morphological ridge (Fig. 2d), suggesting that the underlying ridge and basin morphology predates the majority of sedimentation along the margin (Herzer & Exon 1985). Reflectivity of the ridge and basin

433 sediments changes from chaotic to horizontal and planar with increasing distance from the present-day arc, which
434 suggests that turbiditic flows transport and emplace volcaniclastic material along the forearc (Herzer & Exon
435 1985; Gillies & Davey 1986).

436 In the forward velocity model, the crust beneath the upper-forearc slope is 10-12 ± 0.7 km thick and
437 displays a laterally variable seismic velocity structure (Fig. 6b). Beneath the upper forearc basin, upper- and mid-
438 crust velocities increase from ~3.0 to 6.2 ± 0.3 km s^{-1} over 5 km in depth, and reach 6.8 ± 0.3 km s^{-1} at the base of
439 the crust. Mid-crustal velocities under the morphological ridge are ~2 km shallower than in the basin to the west
440 and increase to ~7.4 ± 0.2 km s^{-1} just above the Moho. Mantle velocities appear to be consistent beneath the
441 forearc, at ~7.8 ± 0.8 km s^{-1}, although poor ray coverage limits model sensitivity in this region (Table 2).

442 Although the inversion model also converged to a solution with high velocity gradients in the shallow
443 crust and a high-velocity lower crust beneath the morphological ridge (Fig. 7c), mantle velocities, >7.8 km s^{-1}, are
444 found ~2 km shallower than in the forward model (Fig. 6b). This is the only significant discrepancy between the
445 forward and inverse velocity models, and coincides with an unusually high FAA, ~150 mGal, which is
446 significantly undercalculated by the density-converted forward velocity model using typical velocity-density
447 relationships (Carlson & Raskin 1984; Christensen & Mooney 1995). Whilst assuming an ~2 km-thinner forearc
448 crust beneath the morphological ridge improves the fit between the observed and calculated datasets, the misfit
449 remains >30 mGal and forward-modelled Moho reflections no longer fit within the assigned uncertainties (Table
450 1). The preferred combined model maintains the crustal thicknesses determined by the forward modelling method,
451 and includes an ~5.0 km-high lower-crustal density anomaly of ~3.2 g cm^{-3} to accurately recreate the forearc FAA,
452 with a misfit of ~13 mGal. The discrepancy in crustal thickness between the forward and inverse velocity models,
453 whilst significant, is within the vertical resolution of the inversion model (Fig. 7e), and most likely results from
454 inversion model smoothing, and the inability to invert Moho-reflected arrivals (P_mP phases – Zelt *et al.* 2003).

455 Both of these scenarios require relatively thin crust compared to previous results from the Tonga, Izu-
456 Bonin-Mariana, and Aleutian margins, although it is not entirely unusual (Fig. 11b). Kodaira *et al.* (2010) imaged
457 <10 km thick forearc crust beneath the Bonin Ridge, attributing the thin crust with forearc spreading during
458 subduction initiation. Similar inferences have been made regarding the origin of the Tonga Ridge, which is widely
459 associated with the onset of west-dipping subduction ~51-48 Ma (Herzer *et al.* 2011; Meffre *et al.* 2012;
460 Michibayashi *et al.* 2012). The forearc structural high observed along Profile B is at the southern end of the
461 bathymetrically expressed Tonga Ridge (Karig 1970; Lonsdale 1986; Contreras-Reyes *et al.* 2011; Stratford *et al.*
462 2015), and most likely also formed during the initial stages of volcanism at the margin. Despite a lack of direct
463 sampling of the lithologies and ages at the southern end of the bathymetrically exposed Tonga Ridge (Clift &
464 MacLeod 1998), evidence from the Profile B MCS section suggests that the ridge-and-basin upper-forearc
465 morphology predates the majority of sedimentation at the margin. As such, we expect the forearc structural high
466 and associated lower-crustal velocity and density anomalies imaged along Profile B to be directly formed by, or
467 developed from, the tholeiitic and boninitic volcanism associated with subduction initiation (Clift *et al.* 1994;
468 Meffre *et al.* 2012; Michibayashi *et al.* 2012; Reagan *et al.* 2013). To achieve the high density and velocity
469 required by the gravity and WA models, the lower crustal structure most likely comprises high-density pyroxenites

that are left as a residual lower-crustal material following initial subduction volcanism (Nakajima & Arima 1998; Meffre *et al.* 2012). We refer to this morphological ridge with high density and seismic velocity, as the extinct Eocene frontal arc.

6 DISCUSSION

6.1 Variations in subducting crust and upper mantle structure

Subduction-induced bending of the downgoing Pacific plate generates large-scale normal faults that are observed along the Tonga-Kermadec margin as significant seabed offsets of up to 2 km (Fig. 9a; Crawford *et al.* 2003), and as downthrown sedimentary units in seismic reflection data (Fig. 10a & b; Pelletier & Dupont 1990). Similar bend faulting is observed into the mantle of the Costa Rican margin (Ranero *et al.* 2003), and pervasively throughout the Chilean trench-outer rise (Contreras-Reyes *et al.* 2008). Along the Chilean margin, the faults coincide with the reduced seismic velocity of the crust, by 0.4-0.7 km s^{-1}, and upper mantle, by up to 0.5 km s^{-1} (Moscoso & Grevemeyer 2015), which are proposed to be the physical manifestation of oceanic crust hydration and upper mantle serpentinisation (e.g. offshore Costa Rica and Nicaragua - Ranero *et al.* 2005 and Ivandic *et al.* 2010, respectively). These pervasive structural and geochemical modifications are attributed with reducing the flexural rigidity of the subducting plate by up to three orders of magnitude over the trench-outer rise region (Billen & Gurnis 2005; Arredondo & Billen 2012). We find that the upper 2 km of the subducting oceanic crust reduces by ~1 km s^{-1} in seismic velocity with increasing proximity to the Tonga-Kermadec trench, over 100-170 km trench-perpendicular distance, whilst no discernable variations are observed in the lower 4 km (Fig. 9b). The seismic velocity of the uppermost mantle reduces by up to 0.5 km s^{-1} for profiles that are roughly perpendicular to the palaeo-spreading direction of the Osbourn spreading centre. This velocity reduction is comparable to that observed at the Central Chile margin (Moscoso & Grevemeyer 2015), but is at the limit of the resolution for the models presented here (Table 2; Contreras-Reyes *et al.* 2010; Contreras-Reyes *et al.* 2011; Stratford *et al.* 2015), so it is not a conclusive result. We note that this velocity reduction is of a similar magnitude to the decrease observed between the upper mantle velocities sampled by profiles perpendicular (Profile A, B, P02, and PCr - Fig. 9) and parallel (Profile P03 - Fig. 9) to the palaeo-spreading direction of the Osbourn spreading centre (Fig. 1) most likely caused by azimuthal mantle anisotropy (Kodaira *et al.* 2014).

Typical bend-related faulting along the Tonga-Kermadec subduction zone is characterised by up to 2 km throw horst-and-graben structures that coincide with a seabed dip of 5°, as shown by Profile D (Fig. 10b – Funnell *et al.* 2014). In the proximity of the present-day LRSC-trench collision zone, the Tonga-Kermadec trench shallows by ~4 km over 150 km (Pontoise *et al.* 1986; Funnell *et al.* 2014), and is coincident with reduced bend-related deformation, as represented by faults observed along Profile B. Faults in this region predominantly form half graben that dip trenchward and exhibit a <0.3 km throw, resulting in the subducting plate remaining sub-horizontal with <1° dip (Fig. 10a). This region of decreased deformation extends up to 120 km from the peak of the closest seamount (Fig. 9a), which is significantly broader than the ~50 km-wide bathymetric swell and lower-crustal support imaged (Fig. 6b; Ballance *et al.* 1989; Contreras-Reyes *et al.* 2010). Although some larger faults

505 are found on the flanks of Osbourn seamount (Stratford *et al*. 2015; Robinson *et al.* in review), the general
506 reduction in subducting plate dip and fault offset suggests that the presence of the LRSC and its corresponding
507 crustal thickening moderates deformation by providing structural and buoyancy-driven support. This also appears
508 to limit the reduction in subducting plate flexural rigidity in the 120 km around the LRSC, resulting in seamounts
509 that effectively subduct on top of a broad raised ridge that would also contribute to deformation of the overriding
510 plate (e.g. Dominguez *et al*. 1998; Zeumann & Hampel 2015).

511 *6.2 Characterising the along-strike variability of the Tonga-Kermadec forearc*

512 The 12-13 km thick forearc-arc crust imaged along Profile B is thin compared to global observations of
513 intra-oceanic overriding crust (Fig. 11a & b). Fig. 12 indicates that the thin crust may not be an isolated feature of
514 the Tonga-Kermadec forearc but part of a trend of northward increasing crustal thickness that reaches >18 km
515 over just 300 km distance along strike (Contreras-Reyes *et al.* 2011). This ~6 km increase is coincident with
516 similar increases in the thickness and width of the high velocity region at the base of the forearc crust, as well as
517 shallowing of the forearc bathymetry. Over the same area, the signature of the FAA (Sandwell *et al.* 2014)
518 increases in amplitude from ~100 mGal around Profile B to >150 mGal at P02 (Fig. 12e), suggesting that one of
519 the dominant controls on the gravity anomaly along the Tonga-Kermadec forearc is the difference in density
520 between lower crustal material associated with the currently active and extinct frontal arc (Fig. 8).

521 The general trend of northward-increasing crustal thickness, the FAA, and the prominence of the extinct
522 Eocene arc appears to continue north and south of the region imaged by Profiles B and A, and profile P02 (Fig.
523 12a & e). To the north, the Eocene frontal arc shoals significantly to form the Tongan island group (Contreras-
524 Reyes *et al.* 2011), and to the south the bathymetric expression disappears beneath the sedimentary basin of the
525 Kermadec forearc whilst the FAA is significantly reduced (Funnell *et al.* 2014). Where sampled, the morphology
526 of the forearc crust indicates that its broad structure predates the majority of sedimentation at the margin (Fig. 2;
527 Herzer & Exon 1985). These observations suggest that the margin-wide trend in forearc crustal thickness is
528 controlled by systematic variations in crustal material generation or erosion following formation, but prior to
529 significant sedimentation and seamount subduction. Such observations fit with the proposed tectonic model of
530 Meffre *et al.* (2012), which infers the southward propagation of subduction initiation, potentially enabling more
531 volcanic material to be generated in the north where subduction has been sustained for a longer period of time.

532 *6.2.1 Southern extent of the extinct Eocene frontal arc*

533 Although the bathymetric expression of the Eocene arc is absent from the Kermadec forearc 50 km south
534 of Profile B, the associated FAA high continues south at a lower amplitude as far as ~31.5°S (Fig. 12e). Using de-
535 trended residual FAA data Bassett *et al.* (2016) show that this termination in gravity signature coincides with the
536 '32°S' tectonic boundary (Ballance *et al.* 1999). This boundary separates a deep sediment-filled basin, a
537 prominent arc, and a typical <3 km-deep backarc basin to the north from a >10 km-deep trench axis and the
538 westward migration of arc volcanism into a deeper, narrower, and more asymmetric Havre Trough (Pelletier &
539 Dupont 1990; Collot & Davy 1998; Ballance *et al.* 1999). Whilst this was initially proposed to result from varying

rates of subduction erosion around the boundary (Pelletier & Dupont 1990; Collot & Davy 1998), more recent research has highlighted the need for a southern limit on the extinct Eocene arc to explain its migration during the opening of the south Fiji Basin (Herzer *et al.* 2012). Based on the absent bathymetric expression and southern termination of the FAA high, we support the interpretation of Bassett *et al.* (2016) that the '32°S' boundary represents the present-day southern limit of the extinct Eocene arc along the Tonga-Kermadec forearc (Fig. 12g).

6.2.2 Northern extent of the extinct Eocene frontal arc

North of Profile P02, the FAA widens and increases in amplitude towards the Tongan islands (Fig. 12e). Just beyond the northern tip of these islands, at ~18°S, there is an abrupt reduction in the FAA, shown as a highly negative vertical gravity gradient (Fig. 12f), which also coincides with an ~2 km-deep bathymetric channel and the broadening and deepening of the forearc and arc (Fig. 12a). This sharp delineation coincides with a decrease in age of dredged rock samples, from 51-39 Ma to 35-28 Ma (Meffre *et al.* 2012), an aseismic discontinuity (Bonnardot *et al.* 2007), and the southern tip of the Fonualei Rift (Zellmer & Taylor 2001; Conder & Wiens 2011). Bonnardot *et al*. (2007) proposed that the initial collision of the LRSC, ~5-4 Ma (Ruellan *et al.* 2003), may have generated this feature, known as the Fonualei Discontinuity (Fig. 1). Although seamount subduction is associated with increased subduction erosion and the removal of significant quantities of material from the overriding plate (Dominguez *et al.* 1998; von Huene *et al.* 2004; Clift & MacLeod 2012), the Fonualei Discontinuity is sharper and extends further arcward than is typically expected for such deformation. The seamount subduction hypothesis also fails to explain the age variation across the boundary. We propose that the Fonualei Discontinuity divides the northern extent of the extinct Eocene frontal arc from a younger volcanic frontal arc to the north (Fig. 12g). The significant broadening and reduction in forearc depth north of the discontinuity compared to the south, by ~1 km (Fig. 12a), may be expected of volcanic arcs at different stages of their evolution (Takahashi *et al.* 2007; Calvert *et al.* 2008; Kodaira *et al.* 2010). Extension along the Fonualei Rift in the Lau Backarc Basin terminates just north of the forearc-dividing discontinuity (Zellmer & Taylor 2001, Conder & Wiens 2011), suggesting that changes in crustal structure not only control forearc deformation, but also backarc stresses and processes as the host structure formed prior to Lau Basin spreading (Pelletier & Louat 1989). The observed lack of seismicity along this discontinuity may be caused by the ability of the forearc crust to accommodate significant stresses due to inherited weaknesses along this boundary.

6.3 Implications for seamount subduction along the Tonga-Kermadec trench

Subduction of bathymetrically prominent ridges and seamounts is commonly associated with increased rates of crustal erosion (Ballance *et al.* 1989; Dominguez *et al.* 1998; Clift & Vannucchi 2004; Zeumann & Hampel 2015). Although early seamount subduction models suggested that flexure of the overriding crust accommodated seamount subduction over a broad region of the forearc (e.g. Scholz & Small 1997), more recent studies find that seamounts deform the overriding forearc in a series of ring and radial faults proximal to the interplate boundary (Dominguez *et al.* 1998; Wang & Bilek 2011).

The ability to determine the exact location of currently subducting seamounts along the Tonga-Kermadec forearc is limited by the morphological complexity of the lower-trench slope (Fig. 9a), and the quality and quantity of data acquired in the region. We find, with the acquisition geometry of Profile B, that the seismic velocity model is only sensitive to changes of >0.5 km s^{-1} in the lower-trench slope region (Fig. 6; Table 2), and that only features larger than 30 km by 3 km may be reliably resolved through inversion modelling (Fig. 7). Such sensitivities are comparable to the perturbation expected by the presence of an intact subducting seamount (Lonsdale 1988; Contreras-Reyes *et al.* 2010), suggesting current WA datasets and associated modelling techniques may be unable to discriminate between the presence and absence of seamounts in the lower-trench slope of the Tonga-Kermadec subduction system.

Despite the current limitations in locating the subducting LRSC beneath the lower-trench slope, the broad-scale and historical influence of seamount subduction on Tonga-Kermadec forearc structure can be more clearly determined. The lower-trench slope crust exhibits low seismic velocities (3-6 km s^{-1}) along the subduction system (Fig. 11c; Crawford *et al.* 2003), suggesting that the region comprises crustal material that has been highly fractured by erosive subduction processes (e.g. von Huene & Ranero 2003; Sallarès & Ranero 2005), although the poor resolution here precludes further analysis. Along Profile B, the ~25 km-wide and relatively flat-topped mid-slope basin is underlain by typical forearc velocities (4-7 km s^{-1}). Similar basins are observed to the south (e.g. Ballance *et al.* 1999; Funnell *et al.* 2014), and north of ~22°S (Wright *et al.* 2000), but are significantly reduced in the vicinity of recent LRSC subduction (Contreras-Reyes *et al.* 2011; Stratford *et al.* 2015). Coincident with this mid-slope basin deformation is a change in the distance between the trench and onset of the Tonga Ridge, or upper-trench slope, which increases from >80 km-trench offset along Profile B to <70 km along Profile A and profile P02 (Fig. 12). Together, these observations support the hypothesis that subduction of the LRSC increases the basal and frontal erosion of the lower-trench slope crustal material (Ballance *et al.* 1989; Contreras-Reyes *et al.* 2011; Stratford *et al.* 2015). The data also suggest that the mid-slope crust and basins, which are typically preserved by steady-state subduction processes (Wright *et al.* 2000), are deformed and removed by stresses either directly as seamounts subduct (Wang & Bilek 2011) or as the inner trench slope re-equilibrates gravitationally through extension and collapse (Clift & Vannucchi 2004; Funnell *et al.* 2014).

These erosional and structural recovery processes that define the subduction of seamounts can thus be used, in the context of the characterised variations in forearc structure (Fig. 12g), to track the effects of LRSC-subduction along the Tonga-Kermadec subduction system. Immediately north of the present-day LRSC-trench intersection point, the Tonga trench reaches its deepest point (10.8 km; Ballance *et al.* 1989), and the trench slopes step westward by up to 80 km (Contreras-Reyes *et al.* 2011). The trench slopes appear to return to a more typical structure around ~23°S (Stratford *et al.* 2015), although the bathymetric ridge and high FAA representative of the extinct Tonga arc exhibits a significant reduction in depth (0.5 km) and amplitude (50 mGal), whilst the trenchward edge of the ridge steps ~20 km westward, at 22°S (Fig. 12). At 22°S the Tonga forearc also displays parallel normal faults that delimit the northern extent of the region of significant faulting and doming observed by Herzer & Exon (1985), which they attribute to extensional stresses active from ~5-1 Ma based on well-tied

seismic data. This suggests that although the Tonga forearc crust thins gradually to the south along the margin (Fig. 12), the pronounced step in forearc structure at this latitude formed as a direct result of seamount subduction-related erosion since ~5 Ma (Ruellan *et al.* 2003; Timm *et al.* 2013), and the subsequent extensional collapse of the forearc to re-establish trench-slope stability. The apparent lack of pervasive deformation north of 22°S (Herzer & Exon 1985; Fig. 12) supports the proposal of Ballance *et al.* (1989) that LRSC-subduction initiated near that latitude and has subsequently migrated southward. The presence of a more westerly trend of the subducted segment of the LRSC than is bathymetrically expressed is thus required to enable sufficient time to pass for the migration, from the onset of subduction at 22°S ~5-4 Ma to the present-day collision zone (Ballance *et al.* 1989; Ruellan *et al.* 2003). Despite the apparent documentation of seamount subduction at ODP site 841 ~1.5 Ma (MacLeod 1994; Clift & MacLeod 1999), there is significant evidence that LRSC seamounts deform a wider region of the complex and faulted lower-trench slopes than expected by their bathymetric expression. This result makes determining the history of seamount subduction more challenging and only with further drill sites along the forearc for comparison would the exact history of seamount subduction at the Tonga-Kermadec margin be reliably determinable.

7 CONCLUSIONS

New WA seismic and density models are synthesised with previously published profiles and satellite-derived gravity maps to highlight along-trench structural variability in the Tonga-Kermadec subducting plate and overriding forearc. We use these observations to characterise inherited forearc structure and determine the spatial and temporal extent of LRSC subduction-related deformation of the overriding plate. We find that:

1. Sampling of the flanks of the LRSC-seamounts fails to image high internal velocities, possibly indicating a laterally limited intrusive mafic core. High seismic velocities, >7.2 km s^{-1}, observed at the base of the crust over 50 km from Canopus seamount suggests their structural support extends over a wide region.
2. Subducting oceanic crust and mantle, which is typically faulted and hydrated as it bends towards the trench resulting in rapid structural weakening, deforms less in the vicinity of the LRSC. Typical bending of the subducting plate generates full graben with up to 2 km vertical throw and a plate dip of <5°, whereas within the vicinity of the LRSC swell, the near-horizontal subducting plate is offset by <200 m dominantly trenchward-dipping normal faults. Shoaling of the trench apex by up to 4 km at the LRSC-trench intersection shows that, despite the limited bathymetric expression of the seamounts, the chain sits atop an ~250 km-wide ridge.
3. The Kermadec forearc comprises lower- and mid-trench slopes that persistently undergo extension due to frontal and basal erosion as well as associated gravitational collapse. Crustal seismic velocities (3.5-6.0 km s^{-1}) are unusually low in this region. Modelling of more typical densities for oceanic crust suggests that they are highly fractured, faulted, and possibly hydrated.
4. The upper forearc slope is dominated by a basin and ridge structure that predates significant sedimentation at the margin. This bathymetric ridge is underlain by high velocities, 7.0-7.4 km s^{-1}, that are best represented by

high density lower-crust (3.2 g cm^{-3}), that most likely formed during subduction initiation along the Tonga-Kermadec margin (~51 Ma).

5. The nature and extent of this Eocene arc can be constrained using the broad-scale high FAA that corresponds to the high density lower crustal anomaly. The extinct arc extends from 32°S to the Fonualei Discontinuity at 18°S, with the overriding crustal thickness increasing to the north.
6. Subduction of the LRSC along the Tonga-Kermadec trench increases the erosion of material from the overriding crust. The lower- and mid-trench slopes are shortened, and the trenchward edge of the Eocene arc most likely undergoes extensional collapse to re-equilibrate trench-slope stability.
7. Although the trench slopes are heavily deformed and eroded as far north as 23°S, extensional faulting of the Tonga forearc crust is observed to 22°S. LRSC-subduction is thus proposed to have begun at 22°S, ~5 Myr ago, although the seamount-associated swell may have enabled a broader footprint of deformation.

ACKNOWLEDGEMENTS

This research project was funded by the Natural Environmental Research Council (NERC) grant NE/F004273/1 (Peirce & Watts 2011). We are grateful to the two anonymous reviewers for their thoughtful and helpful comments on this paper. We would like to thank all involved in the planning and acquisition of data during research cruise S0215, including the officers and crew of the R/V Sonne, the scientific party, and all seagoing technicians. The NERC Ocean-Bottom Instrumentation Facility (Minshull *et al.* 2005) and GEOMAR provided the OBSs used in this project, together with their technical support at sea. The MCS data were processed using Claritas™, and manipulated for plotting using Seismic Unix. All figures were prepared using the Generic Mapping Tools (GMT) package (Wessel & Smith 1998). All data from cruise SO215 are archived at the NERC's British Oceanographic Data Centre, and the final accepted version of this manuscript is available through Durham Research Online (dro.dur.ac.uk).

667 **REFERENCES**

668 Arredondo, K.M. & Billen, M.I., 2012. Rapid weakening of subducting plates from trench-parallel estimates
669 of flexural rigidity, *Phys. Earth Planet. Inter.*, 196–197, 1–13.
670 Aubouin, J. 1989. Some aspects of the tectonics of subduction zones, *Tectonophysics*, 160, 1–21.
671 Ballance, P.F., Scholl, D.W., Vallier, T.L., Stevenson, A.J., Ryan, H. & Herzer, R.H., 1989. Subduction of a late
672 Cretaceous seamount of the Louisville Ridge at the Tonga Trench; A model of normal and accelerated
673 tectonic erosion, *Tectonics*, 8(5), 953–962.
674 Ballance, P.F., Ablaev, A.G., Pushchin, I.K., Pletnec, S.P., Birylina, M.G., Itaya, T., Follas, H.A. & Gibson, G.W.,
675 1999. Morphology and history of the Kermadec-trench-arc-backarc basin-remnant arc system at 30 to
676 32°S: geophysical profile, microfossil and K-Ar data, *Mar. Geol.*, 159, 35–62.
677 Bassett, D. & Watts, A.B., 2015. Gravity anomalies, crustal structure, and seismicity at subduction zones: 1.
678 Seafloor roughness and subducting relief, *Geochem., Geophys. Geosys.*, 16, 1508–1540.
679 Bassett, D., Kopp, H., Sutherland, R., Henrys, S., Watts, A.B., Timm, C., Scherwath, M., Grevemeyer, I. & de
680 Ronde, C.E.J., 2016. Crustal structure of the Kermadec arc from MANGO seismic refraction profile, *J.*
681 *Geophys. Res. Solid Earth*, 121, 7514–7546.
682 Billen, M.I. & Stock, J.M., 2000. Morphology and origin of the Osbourn Trough, *J. Geophys. Res.*, 105, 481-489.
683 Billen, M.I. & Gurnis, M., 2005. Constraints on subducting plate strength within the Kermadec trench, *J. Geophys.*
684 *Res.*, 110, 1–18.
685 Bloomer, S.H., Taylor, B., MacLeod, C.J., Stern, R.J., Fryer, P., Hawkins, J.W. & Johnson, L., 1995. Early arc
686 volcanism and the ophiolite problem: A perspective from drilling in the western Pacific, in *Active*
687 *Margins and Marginal Basins of the Western Pacific*, Geophysical Monograph 88, 1–30.
688 Bonnardot, M.A., Regnier, M., Christova, C., Ruellan, E. & Tric, E., 2007. Seismicity and state of stress within
689 the overriding plate of the Tonga-Kermadec subduction zone, *Tectonics*, 26.
690 Burns, R.E., & Andrews, J.E., 1973. Site 204, *Initial Reports of the Deep Sea Drilling Project*.
691 Calvert, A.J., Klemperer, S.L., Takahashi, N. & Kerr, B.C., 2008. Three-dimensional crustal structure of the
692 Mariana island arc from seismic tomography, *J. Geophys. Res.*, 113, 1–24.
693 Caress, D.W. & Chayes, D.N., 1996. Improved processing of Hydrosweep DS multibeam data on the R/V
694 Maurice Ewing, *Mar. Geophys. Res.*, 18, 631–650.
695 Carlson, R.L. & Raskin, G.S., 1984. Density of the ocean crust, *Nature*, 311, 555–558.
696 Christensen, N.I. & Mooney, W.D., 1995. Seismic velocity structure and composition of the continental crust:
697 A global view, *J. Geophys. Res.*, 100, 9761–9788.
698 Clift, P.D., Bednarz, U., Boe, R., Rothwell, R.G., Hodkinson, R.A., Ledbetter, J.K., Pratt, C.E. & Soakai, S., 1994.
699 Sedimentation on the Tonga forearc related to arc rifting, subduction erosion, and ridge collision: a
700 synthesis of results from sites 840 and 841 *in* Proc. Ocean Drill. Program, Sci. results, Leg 135, 843–
701 855.

Clift, P.D. & MacLeod, C.J., 1998. Tectonic controls on sedimentation and diagenesis in the Tonga Trench and forearc, southwest Pacific, *Geol. Soc. Am. Bull.*, 110, 483–496.

Clift, P.D., MacLeod, C.J., Tappin, D.R., Wright, D.J. & Bloomer, S.H., 1998. Tectonic controls on sedimentation in the Tonga Trench and Forearc, SW Pacific, *Geol. Soc. Am. Bull.*, 110, 483–496.

Clift, P.D. & MacLeod, C.J., 1999. Slow rates of subduction erosion estimated from subsidence and tilting of the Tonga forearc, *Geology*, 27, 411.

Clift, P.D. & Vannucchi, P., 2004. Controls on tectonic accretion versus erosion in subduction zones: Implications for the origin and recycling of the continental crust, *Rev. Geophys.*, *42*.

Collot, J.-Y. & Davy, B., 1998. Forearc structures and tectonic regimes at the oblique subduction zone between the Hikurangi Plateau and the southern Kermadec margin, *J. Geophys. Res.*, 103(B4), 7107.

Conder, J.A. & Wiens D.A., 2011. Shallow seismicity and tectonics of the central and northern Lau Basin, *Earth Planet. Sci. Lett.*, 304, 538–546.

Contreras-Reyes, E., Grevemeyer, I., Flueh, E.R. & Reichert, C., 2008. Upper lithospheric structure of the subduction zone offshore southern Arauco Peninsula, Chile at ~38°S, *J. Geophys. Res.,* 113, B07303.

Contreras-Reyes, E., Grevemeyer, I., Watts, A.B., Planert, L., Flueh, E.R. & Peirce, C., 2010. Crustal intrusion beneath the Louisville hotspot track, *Earth Planet. Sci. Lett.*, 289, 323–333.

Contreras-Reyes, E., Grevemeyer, I., Watts, A.B., Flueh, E.R., Peirce, C., Moeller, S. & Papenberg, C., 2011. Deep seismic structure of the Tonga subduction zone: Implications for mantle hydration, tectonic erosion, and arc magmatism, *J. Geophys. Res.*, 116.

Crawford, W.C., Hildebrand, J.A., Dorman, L.M., Webb, S.C. & Wiens D.A., 2003. Tonga Ridge and Lau Basin crustal structure from seismic refraction data, *J. Geophys. Res.*, 108, 2195.

DeMets, C., Gordon, R.G. & Argus D.F., 2010. Geologically current plate motions, *Geophys. J. Int.*, 181, 1–80.

Dickinson, W.R. & Seely D.R., 1979. Structure and stratigraphy of forearc regions, *Am. Assoc. Pet. Geol. Bull.*, *63*, 2–31.

Dominguez, S., Lallemand, S.E., Malavieille, J. & von Huene R., 1998. Upper plate deformation associated with seamount subduction, *Tectonophysics*, *293*, 207–224.

Downey, N.J., Stock, J.M., Clayton, R.W. & Cande, S.C., 2007. History of the Cretaceous Osbourn spreading center, *J. Geophys. Res.*, 112, 1-18.

Funnell, M.J., Peirce, C., Stratford, W.R., Paulatto, M., Watts, A.B. & Grevemeyer, I 2014. Structure and deformation of the Kermadec forearc in response to subduction of the Pacific oceanic plate, *Geophys. J. Int.*, *199*, 1286–1302.

Gillies, P.N. & Davey, F.J., 1986. Seismic reflection and refraction studies of the Raukumara forearc basin, New Zealand, *New Zeal. J. Geol. Geophys.*, *29*, 391–403.

Hawkins, J.W., Bloomer, S.H., Evans, C.A. & Melchior, J.T., 1984. Evolution of intra-oceanic arc-trench systems, *Tectonophysics*, 102, 175–205.

Hayes, G.P., Wald, D.J. & Johnson, R.L., 2012. Slab1.0: A three-dimensional model of global subduction zone

738 geometries, *J. Geophys. Res.*, 117, B01302.
739 Herzer, R.H. & Exon, N.F., 1985. Structure and Basin Analysis of the Southern Tonga Forear, in *Geology and*
740 *offshore resources of Pacific island arcs—Tonga region, Circum-Pacific Council for Energy and Mineral*
741 *Resources Earth Science Series, v. 2,* Scholl, D.W., and Vallier, T.L.
742 Herzer, R.H., Barker, D.H.N., Roest, W.R. & Mortimer, N., 2011. Oligocene-Miocene spreading history of the
743 northern South Fiji Basin and implications for the evolution of the New Zealand plate boundary,
744 *Geochemistry, Geophys. Geosys.*, 12, doi:10.1029/2010GC003291.
745 Holbrook, W.S., Lizarralde, D., Bangs, N.L. & Diebold, J., 1999. Structure and composition of the Aleutian
746 island arc and implications for continental crustal growth, *Geology*, *27*, 31–34.
747 IOC, IHO and BODC, 2003, "Centenary Edition of the GEBCO Digital Atlas", published on CD-ROM on behalf
748 of the Intergovernmental Oceanographic Commission and the International Hydrographic
749 Organization as part of the General Bathymetric Chart of the Oceans; British Oceanographic Data
750 Centre, Liverpool.
751 Ivandic, M., Grevemeyer, I., Bialas, J. & Petersen, C.J., 2010. Serpentinization in the trench-outer rise region
752 offshore of Nicaragua: Constraints from seismic refraction and wide-angle data, *Geophys. J. Int.*, 180,
753 1253–1264.
754 Karig, D.E., 1970. Ridges and basins of the Tonga-Kermadec Island Arc System, *J. Geophys. Res.*, 75, 239–254.
755 Kodaira, S., Noguchi, N., Takahashi, N., Ishizuka, O. & Kaneda, Y., 2010. Evolution from fore-arc oceanic crust
756 to island arc crust: A seismic study along the Izu-Bonin fore arc, *J. Geophys. Res. Solid Earth*, 115, 1–20.
757 Kodaira, S., Fujie, G., Yamashita, M., Sato, T., Takahashi, T. & Takahashi, N., 2014, Seismological evidence of
758 mantle motions at a palaeo-spreading centre, *Nat. Geosci*., 7, 371-375.
759 Koppers, A., Yamazaki, T., Geldmacher, J., Gee, J.S., Pressling, N. & Hoshi, H., 2012. Limited latitudinal mantle
760 plume motion for the Louisville hotspot, *Nat. Geosci*., 5, 911–918.
761 Lallemand, S.E., Malavieille, J. & Calassou, S., 1992. Effects of oceanic ridge subduction on accretionary
762 wedges: experimental modeling and marine observations, *Tectonics*, 11, 1301–1313.
763 Lonsdale, P.F., 1986. A multibeam reconnaissance of the Tonga trench axis and its intersection with the
764 Louisville guyot chain, *Mar. Geophys. Res.*, 8, 295–327.
765 Lonsdale, P.F., 1988. Geography and history of the Louisville Hotspot Chain in the southwest Pacific, *J.*
766 *Geophys. Res.*, 93, 3078–3104.
767 MacLeod, C.J., 1994. Structure of the outer Tonga forearc at Site 841, *in* Proceedings of the Ocean Drilling
768 Program, *Scientific results, Volume 135:* College Station, Texas, Ocean Driling Program, 373-382.
769 Meffre, S., Falloon, T.J., Crawford, T.J., Duncan, R.A., Bloomer, S.H., & Wright, D.J., 2012. Basalts erupted
770 along the Tongan fore arc during subduction initiation: Evidence from geochronology of dredged rocks
771 from the Tonga fore arc and trench, *Geochem., Geophys. Geosys.*, 13, 1–17.
772 Michibayashi, K., Shinkai, Y., Tani, K., Uehera, S., Harigane, Y., Ishii, T. & Bloomer, S.H., 2012. Tonga Trench
773 gabbros and peridotites: A suit of temporal and spatial forearc materials, *Eos.*, *91*, 1–3.

774 Minshull, T.A., Sinha, M.C. & Peirce, C., 2004. Multi-disciplinary, sub-seabed geophysical imaging – a new
775 pool of 28 seafloor instruments in use by the United Kingdom Ocean Bottom Instrument Consortium,
776 *Sea Technol.*, 46, 27-31.
777 Moscoso, E. & Grevemeyer, I., 2015. Bending-related faulting of the incoming oceanic plate and its effect on
778 lithospheric hydration and seismicity: A passive and active seismological study offshore Maule, Chile, *J.*
779 *Geodyn.*, 90, 58–70.
780 Nafe, J.E. & Drake, C.L., 1957. Variation with Depth in Shallow and Deep Water Marine Sediments of
781 Porosity, and the Velocities of Compressional and Shear Waves, *Geophysics*, 22*,* 523–552.
782 Nakajima, K. & Arima, M., 1998. Melting experiments on hydrous low-K tholeiite: implications for the
783 genesis of tonalitic crust in the Izu-Bonin-Mariana arc, *Island Arc*, 7, 359-373.
784 Peirce, C. & Watts, A.B., 2011. R/V Sonne SO215 Cruise Report. The Louisville Ridge - Tonga Trench
785 collision: Implications for subduction zone dynamics.
786 Pelletier, B. & Louat, R., 1989. Seismotectonics and present-day relative plate motions in the Tonga-Lau and
787 Kermadec-Havre region, *Tectonophysics*, 165, 237–250.
788 Pelletier, B. & Dupont, J., 1990. Erosion, accretion, back-arc extension and slab length along the Kermadec
789 subduction zone, Southwest Pacific, *C. R. Acad. Sci. Paris*, 310, 1657–1664.
790 Pontoise, B., Pelletier, B., Aubouin, J., Baudry, N., Blanchet, R., Butscher, J., Chotin, P., Diament, M., Dupont, M.,
791 Eissen, J., Ferrière, J., Herzer, R., Lapouille, A., Louat, R., d'Ozouville, L., Soakai, S. & Stevenson, A., 1986.
792 Subduction of the Louisville ridge along the Tonga trench: preliminary results of SEAPSO campaign
793 (Leg V), *C. R. Acad. Sc.*, 10, 911–918.
794 Ranero, C.R., Morgan, J.P., McIntosh, K., Reichert, C., 2003. Bending-related faulting and mantle
795 serpentinization at the Middle America trench, *Nature*, 425, 367–73.
796 Ranero, C.R., Villaseñor, A., Morgan, J.P. & Weinrebe, W., 2005. Relationship between bend-faulting at
797 trenches and intermediate-depth seismicity, *Geochem., Geophys. Geosys.*, 6.
798 Reagan, M.K., McClelland, W.C., Girard, G., Goff, K.R., Peate, D.W., Ohara, Y. & Stern, R.J., 2013. The geology of
799 the southern Mariana fore-arc crust: Implications for the scale of Eocene volcanism in the western
800 Pacific, *Earth Planet. Sci. Lett.*, 380, 41–51.
801 Richards, M., Contreras-Reyes, E., Lithgow-bertelloni, C., Ghiorso, M. & Stixrude, L., 2013. Petrological
802 interpretation of deep crustal intrusive bodies beneath oceanic hotspot provinces, *Geochem., Geophys.*
803 *Geosys.*, 14, 604–619.
804 Robinson, A.H., Peirce, C. & Funnell, M.J., (*in review*). Crustal structure of the Louisville Ridge – an insight
805 into the life cycle of seamounts, *Geophys. J. Int.*
806 Ruellan, E., Delteil, J., Wright, I. & Matsumoto T., 2003. From rifting to active spreading in the Lau Basin -
807 Havre Trough backarc system (SW Pacific): Locking/unlocking induced by seamount chain subduction,
808 *Geochem., Geophys. Geosys.*, 4.
809 Sallarès, V. & Ranero C.R., 2005. Structure and tectonics of the erosional convergent margin off Antofagasta,

north Chile (23°30′S), *J. Geophys. Res. B Solid Earth*, 110, 1–19.

Sandwell, D.T., Muller, R.D., Smith, W.H.F., Garcia, E.S. & Francis R., 2014. New global marine gravity model from CryoSat-2 and Jason-1 reveals buried tectonic structure, *Science*, 65, 1–4.

Scholz, C.H. & Small, C., 1997. The effect of seamount subduction on seismic coupling. *Geology*, 25, 487–490.

Spudich, P. & Orcutt, J., 1980. A new look at the seismic velocity structure of the oceanic crust, *Reviews of Geophysics and Space Physics,* 18**,** 627-645.

Stratford, W.R., Peirce, C., Paulatto, M., Funnell, M.J., Watts, A.B., Grevemeyer, I. & Bassett D., 2015. Seismic velocity structure and deformation due to the collision of the Louisville Ridge with the Tonga-Kermadec Trench, *Geophys. J. Int.*, 200, 1503–1522.

Takahashi, N., Kodaira, S., Klemperer, S.L., Tatsumi, Y., Kaneda, Y. & Suyehiro K., 2007. Crustal structure and evolution of the Mariana intra-oceanic island arc, *Geology*, 35, 203–206.

Takahashi, N., Kodaira, S., Tatsumi, Y., Yamashita, M., Sato, T., Kaiho, Y., Miura, S., No, T., Takizawa, K. & Kaneda Y., 2009. Structural variations of arc crusts and rifted margins in the southern Izu-Ogasawara arc-back arc system, *Geochem., Geophys. Geosys.*, *10*.

Talwani, M., Worzel, J.L. & Landisman M., 1959. Rapid gravity computations for two-dimensional bodies with application to the Mendocino submarine fracture zone, *J. Geophys. Res.*, 64, 49–59.

Timm, C., Bassett, D., Graham, I.J., Leybourne, M.I., de Ronde, C.E.J., Woodhead, J., Layton-Matthews, D. & Watts, A.B., 2013. Louisville seamount subduction and its implication on mantle flow beneath the central Tonga-Kermadec arc, *Nat. Commun.*, 4, 1720.

Vanderkluysen, L., Mahoney, J.J., Koppers, A.A.P., Beier, C., Regelous, M., Gee, J.S. & Lonsdale, P.F., 2014. Louisville Seamount Chain: Petrogenetic processes and geochemical evolution of the mantle source, *Geochemistry, Geophys. Geosystems*, 15, 1–21.

von Huene, R. & Scholl, D.W., 1991. Observations at convergent margins concerning sediment subduction, subduction erosion, and the growth of continental crust, *Rev. Geophys.*, *29*, 279–316.

von Huene, R., Corvalán, J., Flueh, E.R., Hinz, K., Korstgard, J., Ranero, C.R. & Weinrebe, W., 1997. Tectonic control of the subducting Juan Fernández Ridge on the Andean margin near Valparaiso, Chile, *Tectonics*, *16*, 474–488.

von Huene, R. & Ranero C.R., 2003. Subduction erosion and basal friction along the sediment-starved convergent margin off Antofagasta, Chile, *J. Geophys. Res.*, *108*, 2079.

von Huene, R., Ranero, C.R. & Vannucchi P., 2004. Generic model of subduction erosion, *Geology*, 32, 913–916.

Wang, K. & Bilek, S.L., 2011. Do subducting seamounts generate or stop large earthquakes? *Geology*, 39, 819–822.

Watts, A.B., Peirce, C., Grevemeyer, I., Paulatto, M., Stratford, W.R., Bassett, D., Hunter, J.A., Kalnins, L.M. & de Ronde C.E.J., 2012. Rapid rates of growth and collapse of Monowai submarine volcano in the Kermadec Arc, *Nat. Geosci.*, 5, 510–515.

Wessel, P. & Smith, W., 1998. New, improved version of Generic Mapping Tools released, *Eos.*, *79*, 579.

White, R.S., Mckenzie, D. & O'Nions R.K., 1992. Oceanic crustal thickness from seismic measurements and rare earth element inversions, *J. Geophys. Res.*, *97*, 683–715.

Wright, D.J., Bloomer, S.H., MacLeod, C.J., Taylor, B. & Goodlife, A.M., 2000. Bathymetry of the Tonga Trench and Forearc: a map series, *Mar. Geophys. Res.*, 21, 489–511.

Zellmer, K.E. & Taylor, B., 2001. A three-plate kinematic model for Lau Basin opening, *Geochem., Geophys. Geosys.*, *2*.

Zelt, C.A., 1998. Lateral velocity resolution from three-dimensional seismic refraction data, *Geophys. J. Int.*, 135, 1101–1112.

Zelt, C.A. & Ellis, R.M., 1988. Practical and efficient ray tracing in two-dimensional media for rapid traveltime and amplitude forward modelling, *Can. J. Explor. Geophys.*, 21, 16–31.

Zelt, C.A. & Smith, R.B., 1992. Seismic traveltime inversion for 2-D crustal velocity structure, *Geophys. J. Int.*, 108, 16–34.

Zelt, C.A. & Barton, P.J., 1998. Three-dimensional seismic refraction tomography: A comparison of two methods applied to data from the Faeroe Basin, *J. Geophys. Res. Solid Earth*, 103, 7187–7210.

Zelt, C.A., Sain, K., Naumenko, J.V. & Sawyer, D.S., 2003. Assessment of crustal velocity models using seismic refraction and reflection tomography, *Geophys. J. Int.,* 153, 609-626.

Zeumann, S. & Hampel, A., 2015. Deformation of erosive and accretive forearcs during subduction of migrating and non-migrating aseismic ridges: Results from 3-D finite element models and application to the Central American, Peruvian, and Ryukyu margins, *Tectonics*, 34, 1769–1791.

866 **TABLE 1**

Model region	Phase	Average uncertainty (ms)	Number of picks	T_{RMS} misfit (ms)	χ^2
Pacific plate	P_g	37	6,362	45	1.20
	P_mP	43	4,643	51	1.25
	P_n	51	15,199	109	1.94
Trench	P_g	47	1,748	71	1.73
	P_mP	59	728	83	2.11
	P_n	72	3,291	145	3.79
Forearc	P_s	26	133	21	0.54
	P_g	40	6,155	78	2.86
	P_mP	48	2,863	64	1.87
	P_n	48	4,183	98	1.67
Full model	P_s	27	133	21	0.54
	P_g	40	14,265	62	1.98
	P_mP	48	8,234	58	1.54
	P_n	54	22,673	112	2.16
Overall values:	**-**	**-**	**45,305**	**86**	**1.98**

867

868 Table 1. Summary of picked and modelled phases. The final model compares over 45,000 modelled arrivals to
869 observed phases, with a combined $\chi^2<2$. Phases through different model sections, as well as the final model as a
870 whole, are listed separately to highlight the disparity in data quality and modelling capabilities along the profile.

871 **TABLE 2**

Layer	Model side	Forearc, OBSs 1-10, $\chi \leq 3.5$			
		Lower ΔZ (km)	Upper V_p (km s^{-1})	Lower V_p (km^{-1})	Const. V_p grad.
Sediment	Forearc	0.1	0.3	0.2	0.1
Crust	Forearc	0.5	0.3	0.3	0.1
Mantle	Forearc	-	0.8	0.3	0.2

Layer	Model side	Trench, OBSs 11-15, $\chi \leq 3.5$			
		Lower ΔZ (km)	Upper V_p (km s^{-1})	Lower V_p (km^{-1})	Const. V_p grad.
Sediment	Both	-	-	-	-
Crust	Forearc	-	0.6	0.7	0.6
Mantle	Forearc	-	0.2	0.2	0.6
Crust	Pacific plate	-	0.5	0.3	0.4
Mantle	Pacific plate	-	0.2	0.1	-

Layer	Model side	Pacific plate, OBSs 16-27, $\chi \leq 2$			
		Lower ΔZ (km)	Upper V_p (km s^{-1})	Lower V_p (km^{-1})	Const. V_p grad.
Sediment	Pacific plate	0.1	0.5	0.3	0.2
Crust	Pacific plate	0.3	0.3	0.3	0.2
Mantle	Pacific plate	-	0.3	0.1	0.1

872

873 Table 2. Summary of results from independently testing the sensitivity of different final forward model sections.
874 Control tests, in which rays from a subset of instruments were traced through the unedited respective model
875 sections, indicated the contribution of each set to the overall model fit. Crustal layer sensitivities are presented in
876 this table as the average of the three layers, rather than as individual values, for brevity and thus may vary from
877 values quoted in the text. ΔZ and V_p signify change in depth and P-wave seismic velocity, respectively. Note that
878 layer thicknesses were not tested in the trench section because of model complexity.

879 **FIGURE 1**

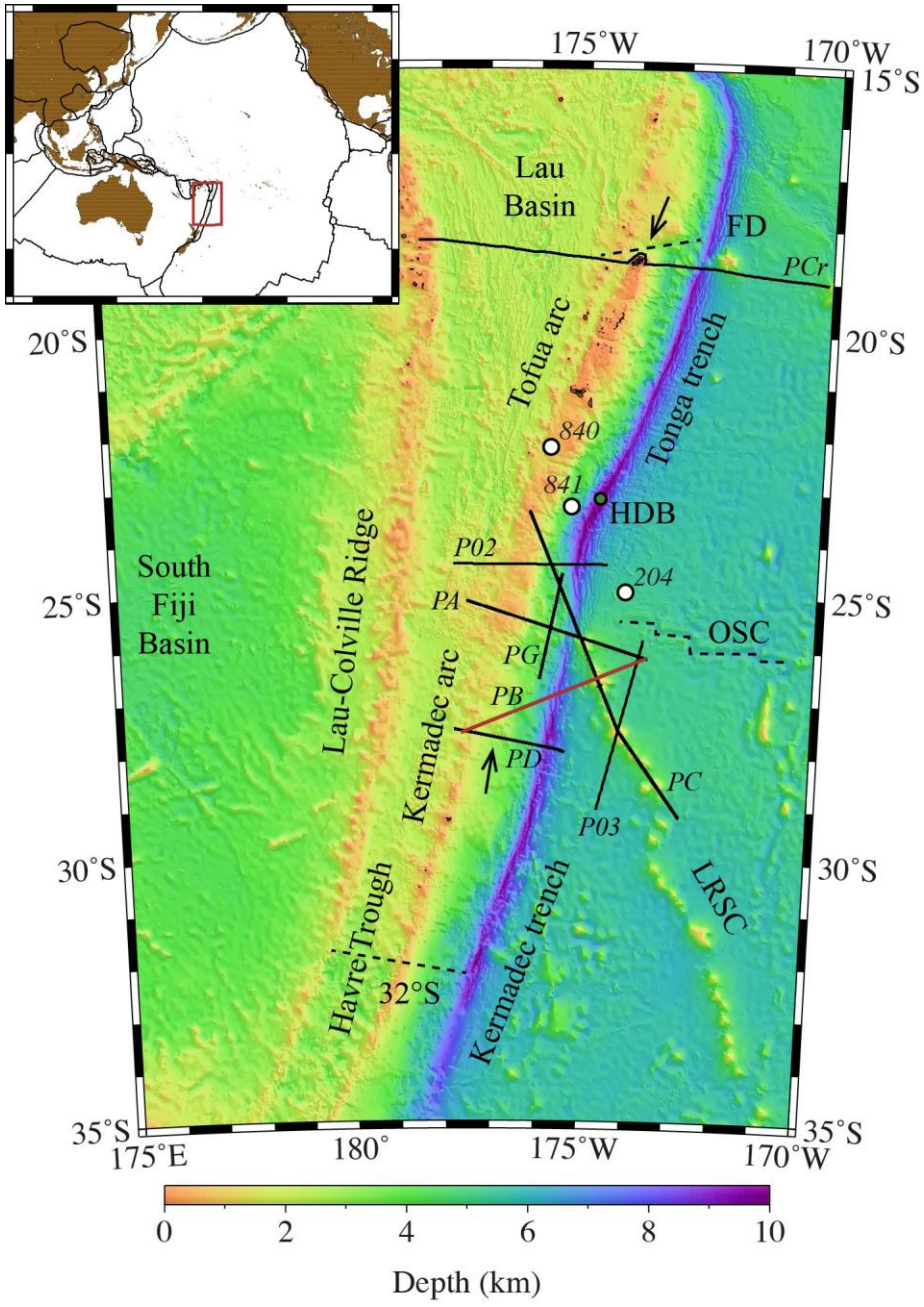

880

881 Fig. 1. Regional bathymetric map of the Tonga-Kermadec subduction system and the northwestern end of the
882 LRSC (IOC *et al.* 2003). All major tectonic features are labelled, and black arrows highlight the extent of the
883 bathymetrically expressed extinct Tonga arc. FD, LRSC, OSC, and HDB (green circle) represent the Fonualei
884 Discontinuity, Louisville Ridge Seamount Chain, Osbourn spreading centre, and Horizon Deep Bight respectively.
885 Labelled black and red lines represent existing geophysical profiles and Profile B (PB), the focus of this study,
886 respectively. White circles indicate locations of numbered ODP and DSDP drill sites (Burns & Andrews 1973;
887 Clift *et al.* 1994).

888 **FIGURE 2**

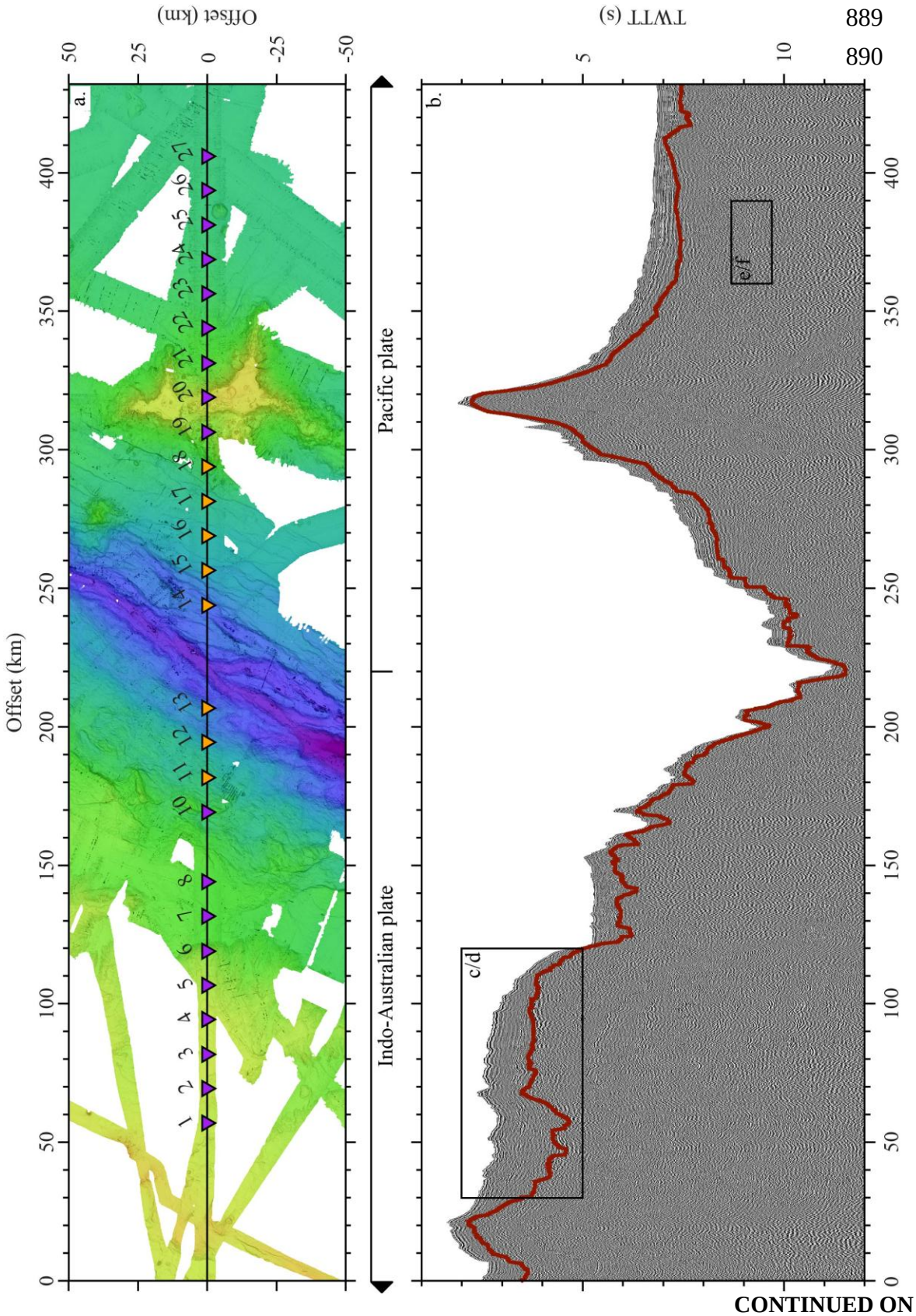

889
890
891

CONTINUED ON NEXT PAGE

892 **FIGURE 2 CONTINUED**

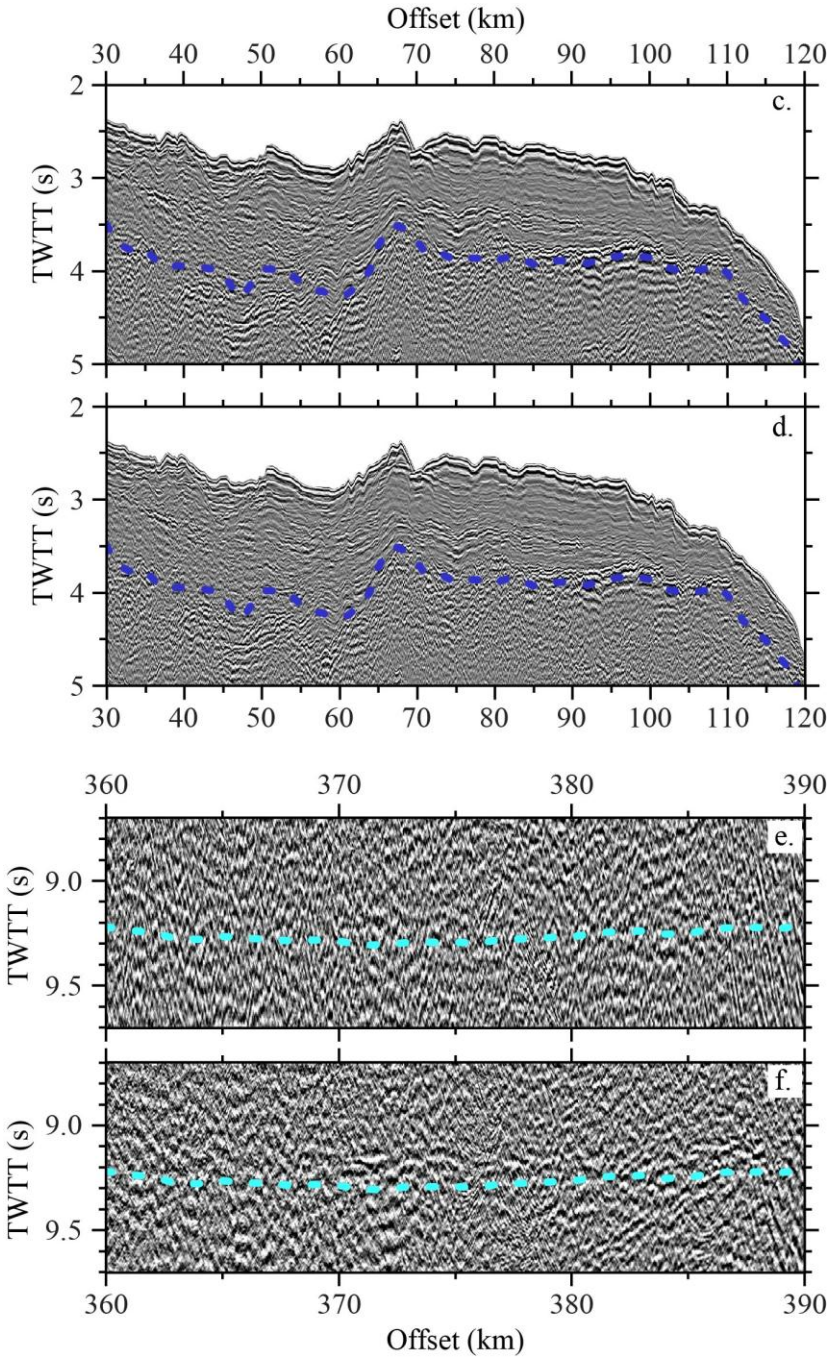

893

894 Fig. 2. Overview of geophysical data acquired along Profile B. a) Swath bathymetry map with LC- (purple) and
895 KUM-type (orange) ocean-bottom seismographs marked on Profile B (black line). b) Fully processed MCS
896 section with major region classifications above, and the interpreted base-sediment reflector shown by the red line.
897 c) First-pass velocity model-stacked MCS data over the Kermadec forearc ridge. d) Final WA velocity model-
898 restacked data over the same region as c). Dark blue dots indicate the forward WA model sediment-crust interface.
899 e) First-pass velocity model stack. f) Final WA velocity model-restacked MCS data highlighting the improved
900 clarity of the Moho reflector and its fit with the Moho of the forward velocity model (light blue dots).

FIGURE 3

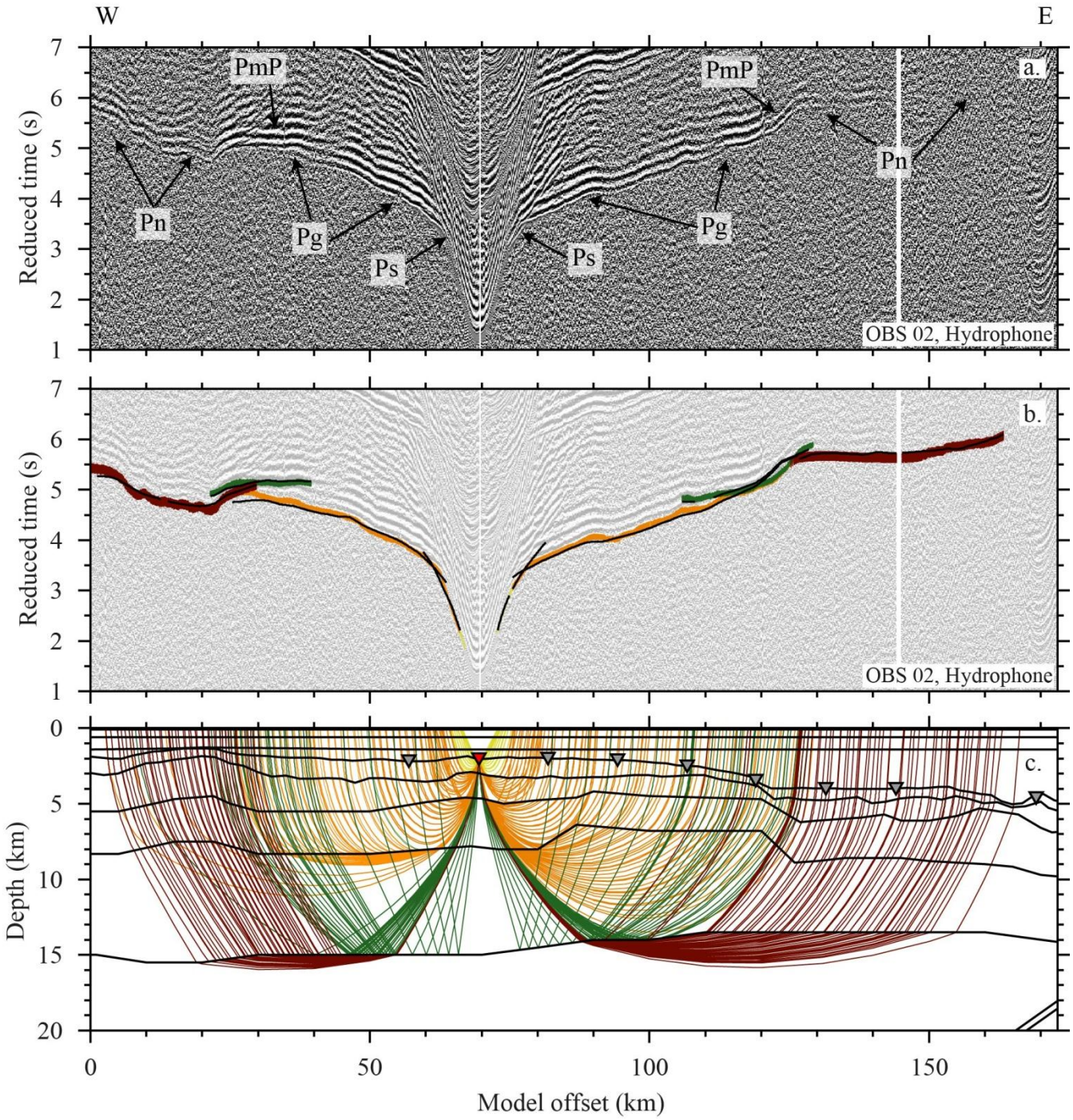

Fig. 3. Kermadec forearc. a) Hydrophone data from OBS 02 plotted with a reduction velocity of 8 km s^{-1}, with major phases labelled. b) Picked phases (yellow – P_s; orange – P_g; green – P_mP; brown – P_n). Colour bar height indicates pick uncertainty, and black lines represent modelled arrival traveltimes. c) Calculated ray-paths for each picked phase through the final forward model. The location of OBS 02 is indicated by the red inverted triangle.

907 **FIGURE 4**

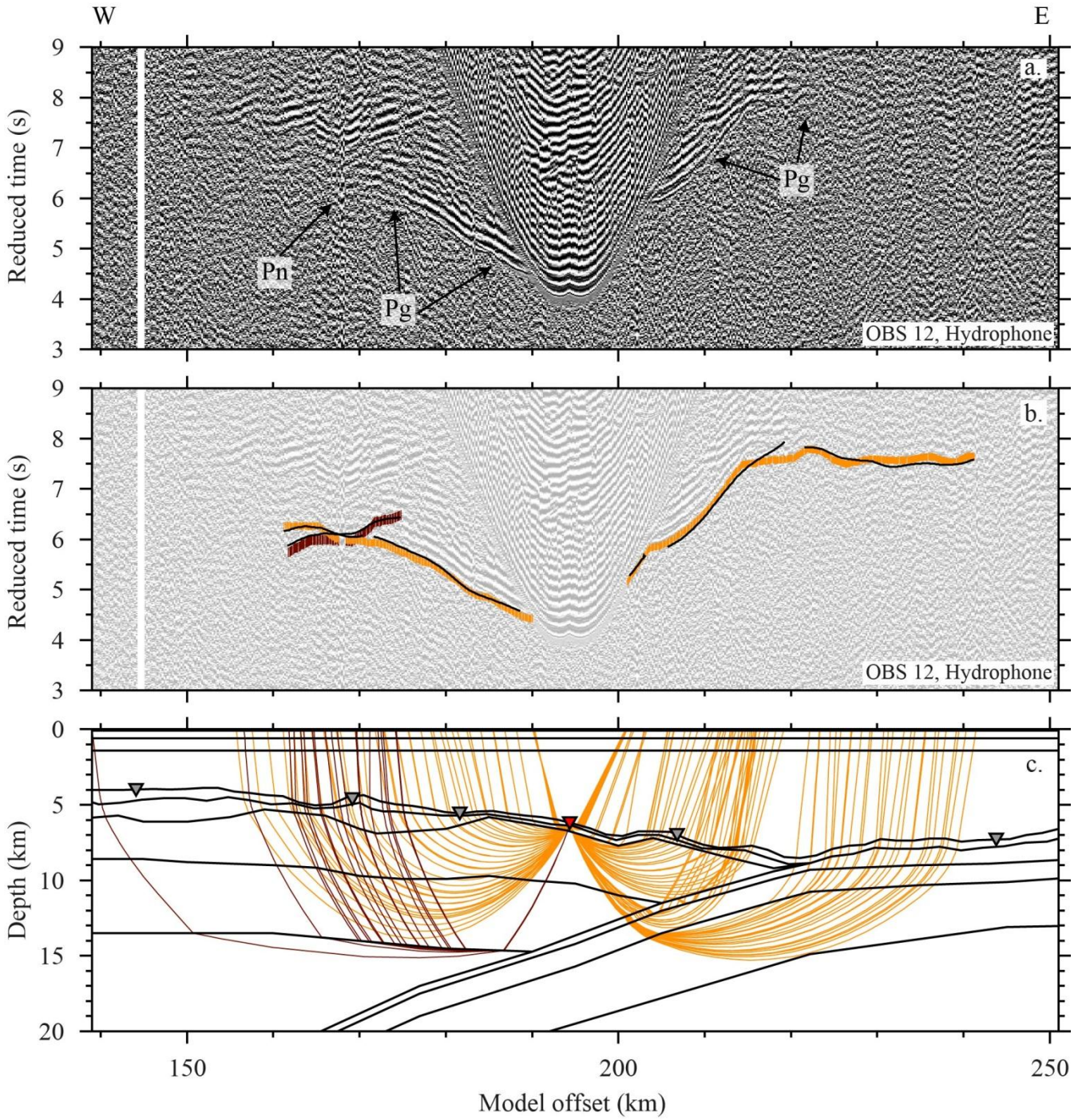

908

909 Fig. 4. Kermadec trench. a) Hydrophone data from OBS 12 plotted with a reduction velocity of 8 km s^{-1}, with
910 major phases labelled. b) Picked phases (yellow – P_s; orange – P_g; green – P_mP; brown – P_n). Colour bar height
911 indicates pick uncertainty, and black lines represent modelled arrival traveltimes. c) Calculated ray-paths for each
912 picked phase through the final forward model. The location of OBS 12 is indicated by the red inverted triangle.

913 **FIGURE 5**

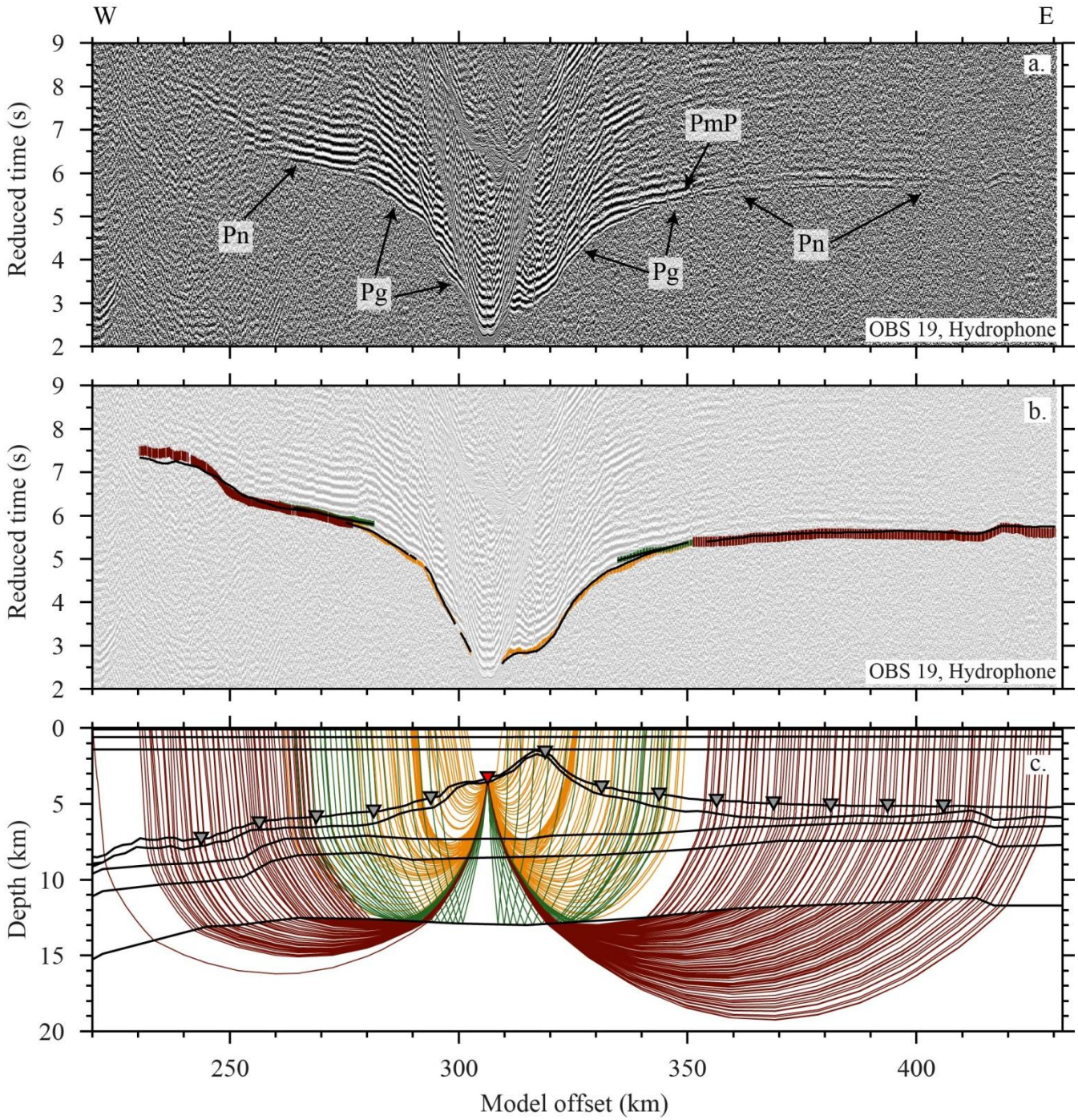

914
915

916 Fig. 5. Pacific plate a) Hydrophone data from OBS 19 plotted with a reduction velocity of 8 km s^{-1}, with major
917 phases labelled. b) Picked phases (yellow – P_s; orange – P_g; green – P_mP; brown – P_n). Colour bar height indicates
918 pick uncertainty, and black lines represent modelled arrival traveltimes. c) Calculated ray-paths for each picked
919 phase through the final forward model. The location of OBS 19 is indicated by the red inverted triangle.

920 **FIGURE 6**

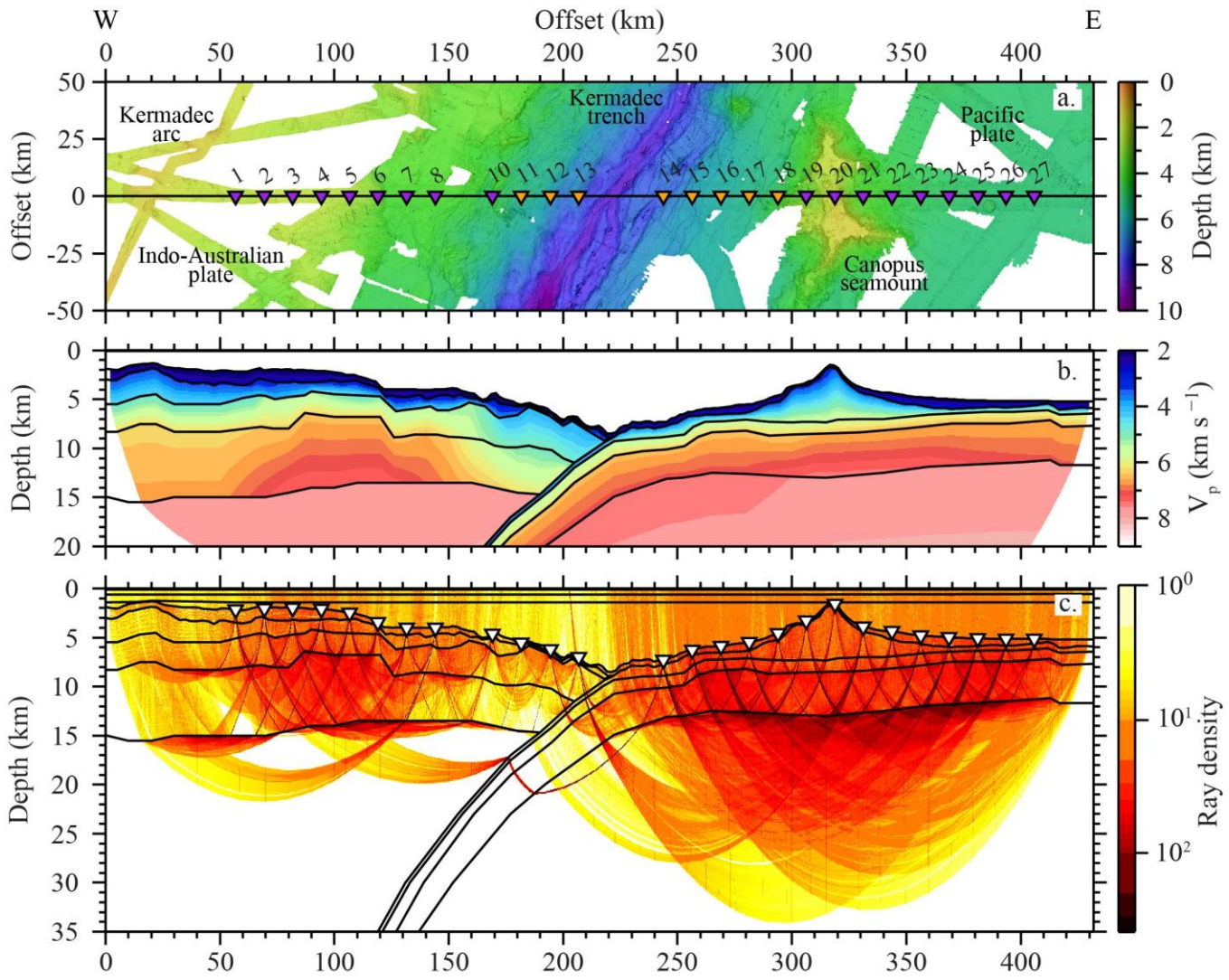

921
922

923 Fig. 6. a) Location of OBSs along Profile B. b) Final forward velocity model for Profile B, with layer boundaries
924 marked in black. c) Traced-ray density through the forward model space. Model misfits are indicated in Table 1,
925 and the sensitivity of the model fit to boundary perturbations is highlighted in Table 2.

926 **FIGURE 7**

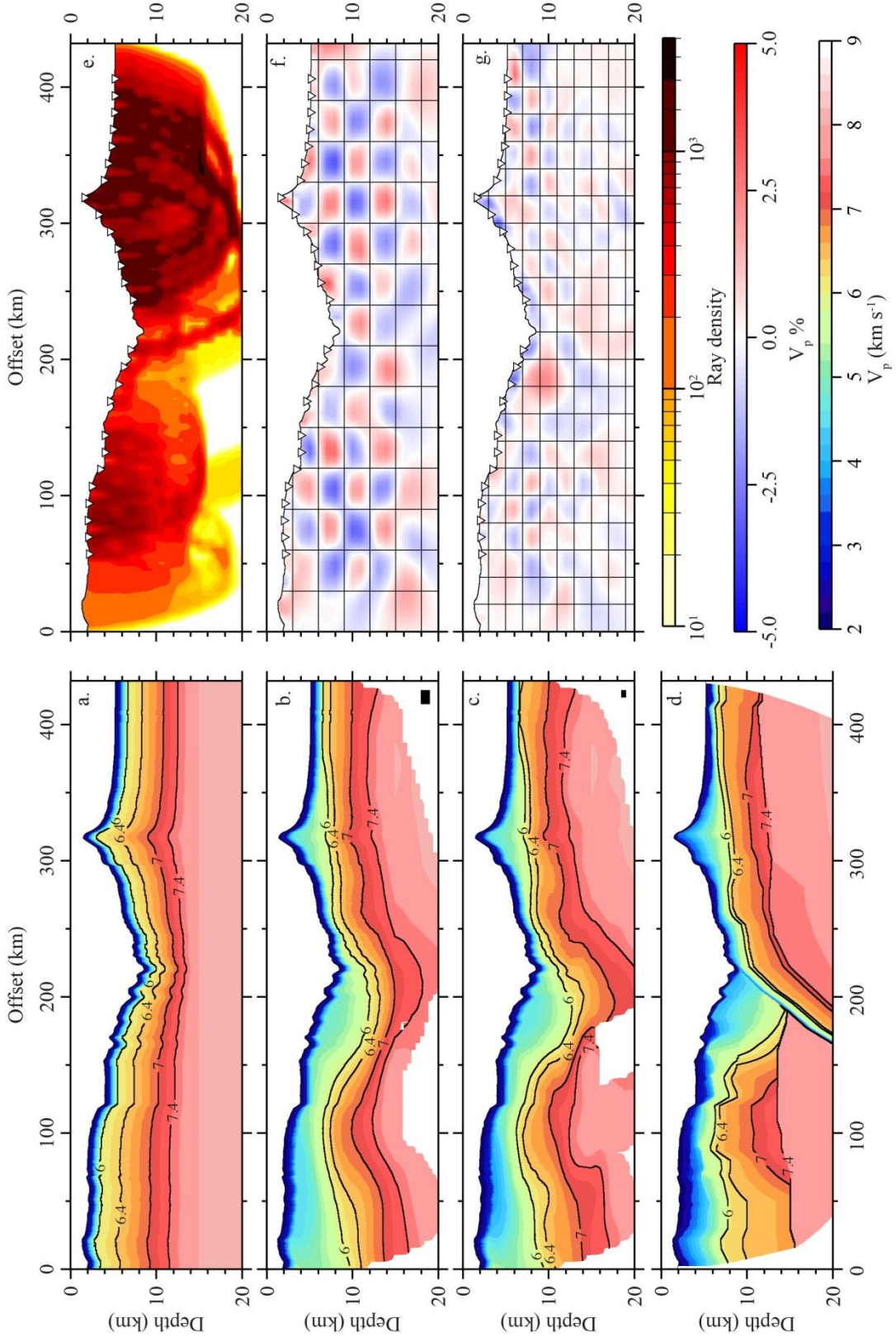

927

928 Fig. 7. a) Initial inversion model with velocities increasing to 8 km s^{-1} at 15 km-depth. Velocity contours for a-d
929 are annotated in km s^{-1}. b) Result from the first run of five non-linear inversions on the initial model, using a 10

930 km by 1 km inversion cell size. c) Final result, following a further five non-linear inversions of the result of the
931 first run, using a 5 km by 0.5 km inversion cell size. The box in the bottom-right hand corner of b) and c) indicates
932 inversion cell sizes for each model space. d) Final forward WA velocity model from Fig. 6, with the same
933 velocities contoured for comparison with parts a-c. e) Final velocity model inversion ray density. f) 30 km by 3
934 km checkerboard test result, showing good anomaly recovery to ~16 km depth and within 20 km of the model
935 edges. The black grid lines indicate the input checkerboard dimensions. g) 20 km by 2 km checkerboard test
936 result, indicating good recoverability is limited to within the subducting plate and between 50-150 km offset in the
937 overriding crust.

938 **FIGURE 8**

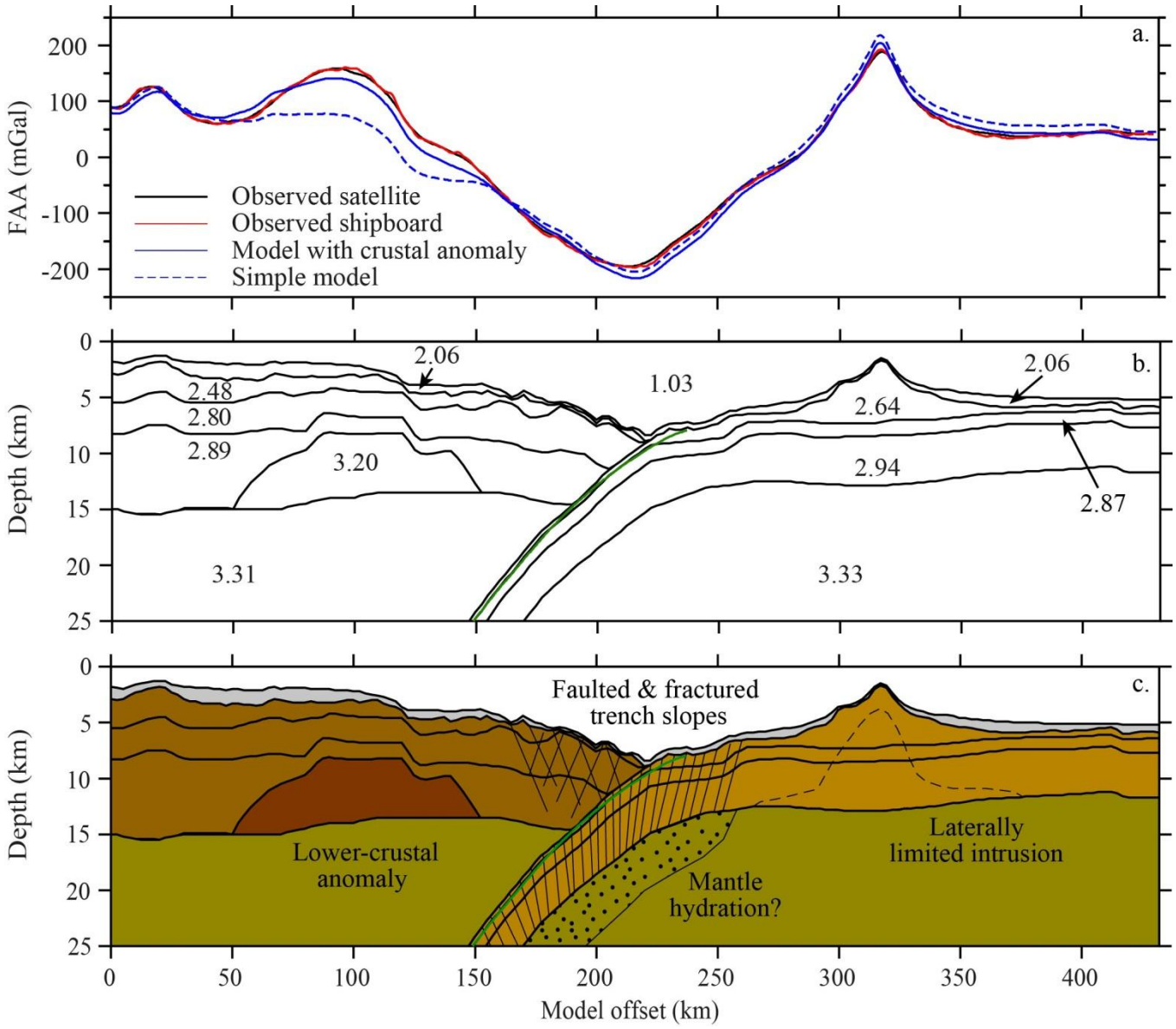

939
940

941 Fig. 8. a) Observed satellite- and shipboard-derived free air anomalies (FAA) compared to the calculated
942 anomalies from different density models. b) Layered block model, with lower-crustal high-density structure.
943 Values denote assigned block density (expressed in g cm^{-3} for brevity and clarity of annotation). c) Combined
944 geophysical model and structural interpretation along Profile B. The green line in parts b) and c) depicts the
945 slab1.0 model projected along Profile B (Hayes *et al.* 2012).

946 **FIGURE 9**

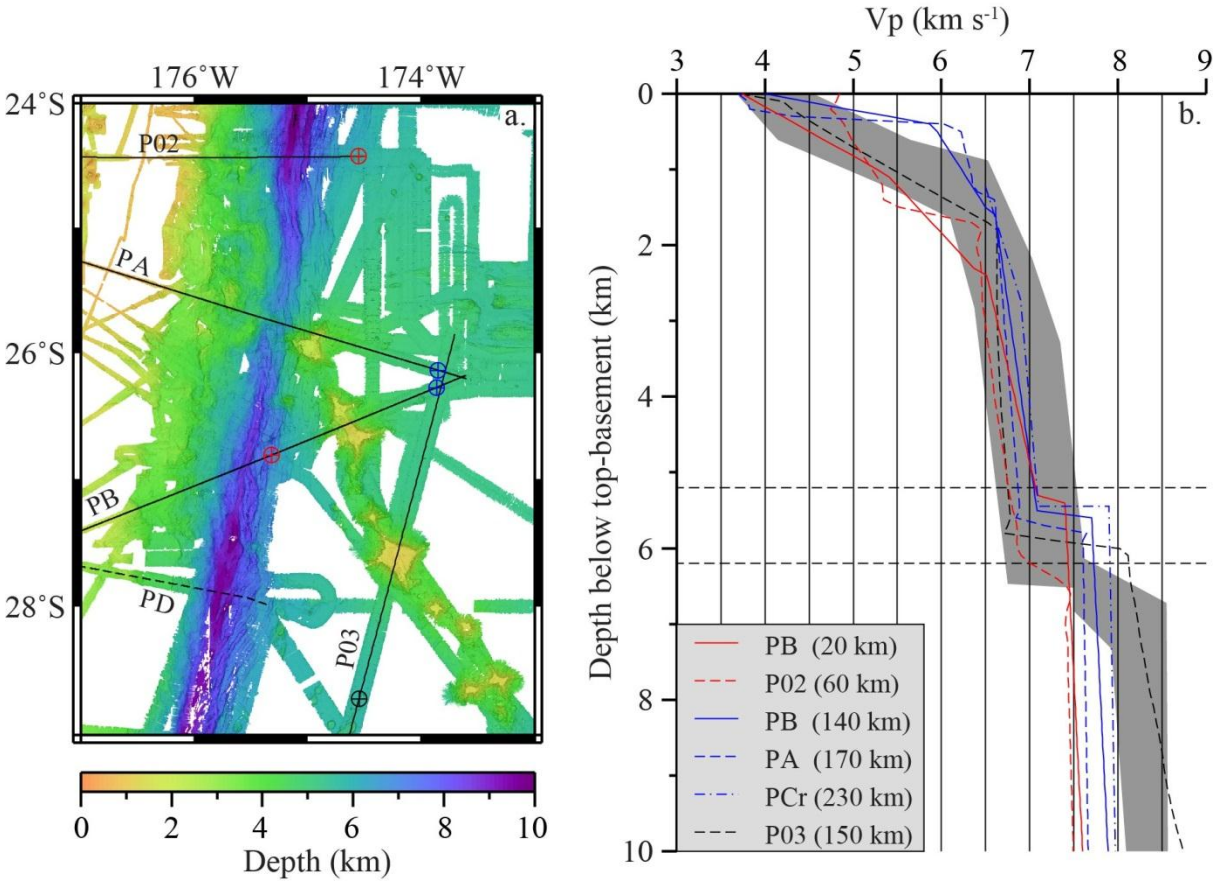

947

948 Fig. 9 a) Bathymetric map of the Pacific plate in the vicinity of the LRSC-Tonga trench collision zone. WA
949 profiles, and the locations of the 1D seismic velocity profiles, presented in b), are indicated by lines and circles,
950 respectively. Profile names are annotated (Profile A is PA, etc.) b) Velocity profiles through the crust and mantle.
951 The grey-shaded region represents average seismic velocities for mature Pacific oceanic crust (>25 Ma) from
952 White *et al.* (1992).

953 **FIGURE 10**

954

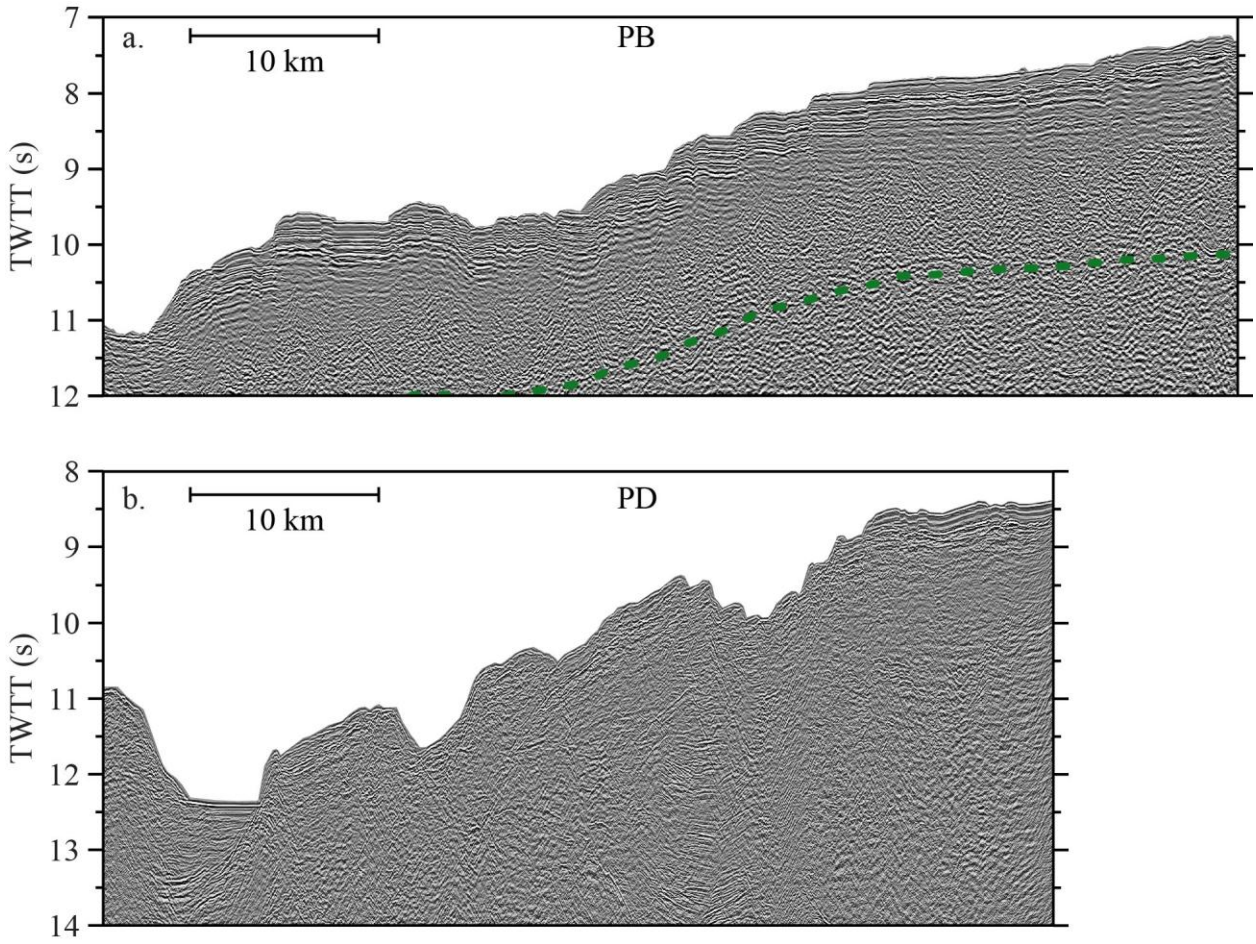

955
956

957 Fig. 10. a) and b) MCS data from the trench-proximal Pacific crustal regions of Profiles B and D respectively
958 (Fig. 9a), highlighting the varying nature of normal faulting along the margin. Green dots on the Profile B MCS
959 data indicate the TWTT of the final forward velocity model crust-mantle layer boundary.

960 **FIGURE 11**

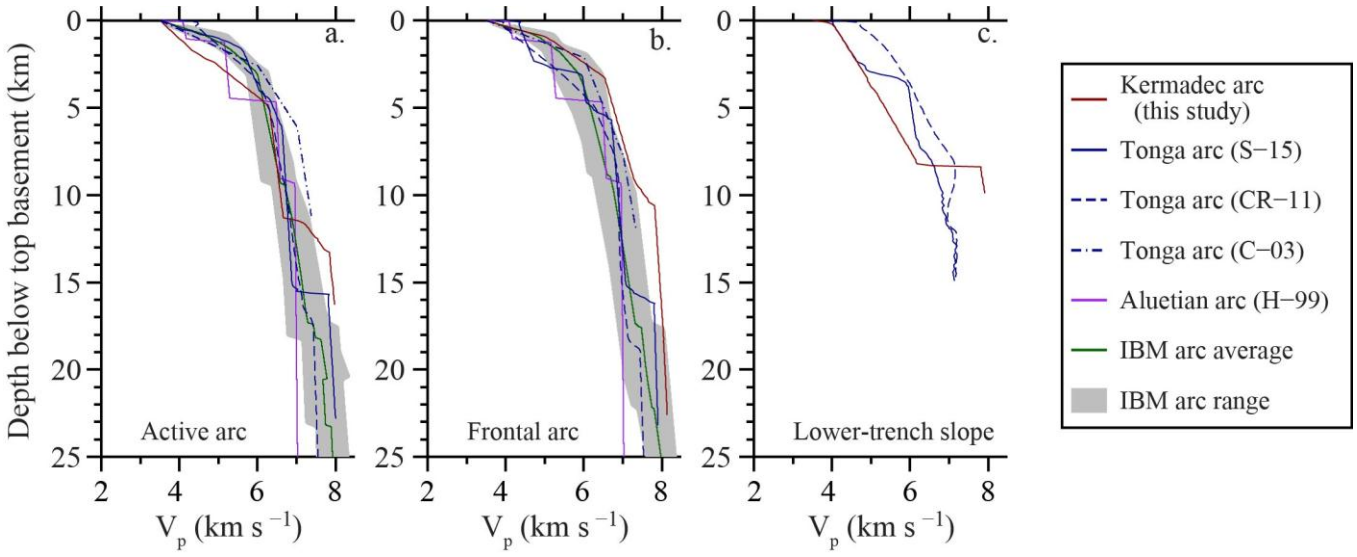

961
962

963 Fig. 11. a), b) & c) 1D velocity profiles through the crust and upper mantle of the active arc, frontal inactive arc,
964 and lower trench slopes respectively. 1D profiles presented are, S-15, from Stratford *et al.* (2015), CR-11, from
965 Contreras-Reyes *et al.* (2011), C-03, from Crawford *et al.* (2003), and H-99, from Holbrook *et al.* (1999). The Izu-
966 Bonin-Mariana range and average 1D-seismic velocity profiles are derived from a compilation of published results
967 from across the margin, including Takahashi *et al.* (2007), Calvert *et al.* (2008), Takahashi *et al.* (2009), Kodaira
968 *et al.* (2010).

969 **FIGURE 12**

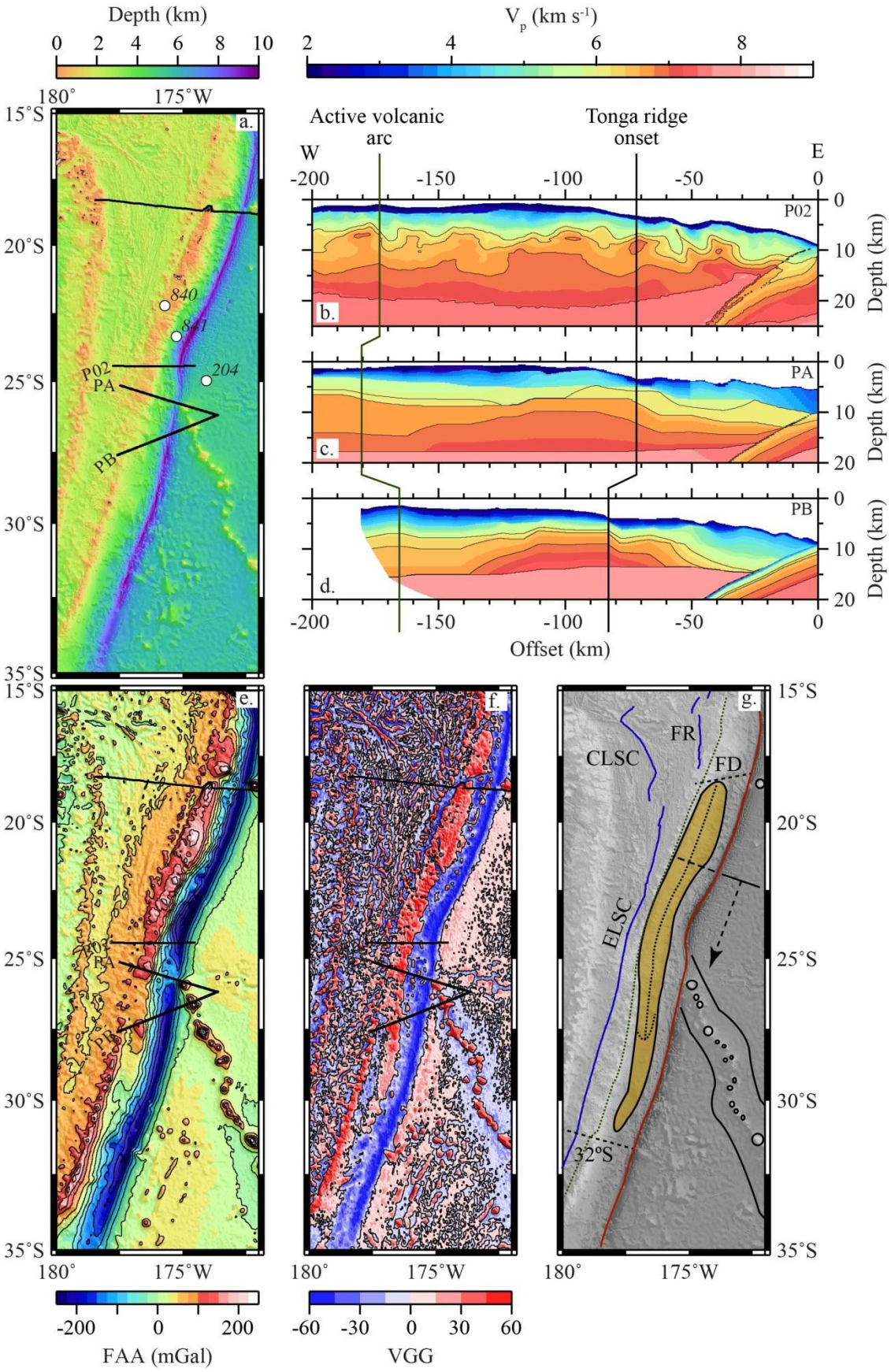

970

Fig. 12. Maps and WA seismic velocity models highlighting variable forearc structure along the Tonga-Kermadec subduction system. a) Regional bathymetry map, with relevant WA profiles labelled. b), c), and d) Trench-oriented and perpendicular distance offset (arcwards negative) WA seismic profiles presented at the same scale for comparison. Profile P02 (P02) data are from Contreras-Reyes *et al.* (2011), Profile A (PA) from Stratford *et al.* (2015), and Profile B (PB) from this study. Forearc crust generally thickens from Profile B to P02. e) Regional FAA. f) Vertical gravity gradient (VGG), which highlights the extent of the extinct Tonga Ridge beneath the forearc between 18 and 32°S as a highly positive gravity gradient. g) Summary of along-arc changes in forearc and arc structure, highlighting major tectonic boundaries and regions of LRSC deformation. Annotated features are: the Central and Eastern Lau Spreading Centres (CLSC and ELSC, respectively), the Fonualei Rift (FR), and the Fonualei Discontinuity (FD).